LUND UNIVERSITY

Scattering from a multilayered sphere - Applications to electromagnetic absorbers on double curved surfaces

Ericsson, Andreas; Sjöberg, Daniel; Larsson, Christer; Martin, Torleif

2017

Scattering from a multilayered sphere - Applications to electromagnetic absorbers on double curved surfaces

Andreas Ericsson, Daniel Sjöberg, Christer Larsson, and Torleif Martin

Electromagnetic Theory
Department of Electrical and Information Technology
Lund University
Sweden

Andreas Ericsson
andreas.ericsson@eit.lth.se

Department of Electrical and Information Technology
Electromagnetic Theory
Lund University
P.O. Box 118
SE-221 00 Lund
Sweden

Daniel Sjöberg
daniel.sjoberg@eit.lth.se

Department of Electrical and Information Technology
Electromagnetic Theory
Lund University
P.O. Box 118
SE-221 00 Lund
Sweden

Abstract

The scattering from a layered sphere with any number of layers and admittance sheets at the interfaces is calculated in this work. By utilizing spherical vector wave expansion and matching of the tangential fields at each interface, and introducing a surface admittance to the magnetic field boundary condition, the transition matrix components are determined. A numerical implementation of the derived analytic expressions is utilized to determine the monostatic radar cross section from a sphere, of varying radius, coated with a number of different electromagnetic absorbers. When the monostatic scattering from a sphere coated by an absorber is normalized with the monostatic scattering, either from the uncoated structure or from an enclosing perfect electric conductor, a comparison can be made to the planar absorber performance. The impact of curvature on the absorber performance is evaluated from these results. It is concluded that absorbers based on bulk losses are less sensitive to curvature than absorbers based on single or multiple layers of thin sheets.

1 Introduction

Electromagnetic scattering from a sphere is a subject with a long and distinguished history. It can be argued who was first in presenting a solution to the problem, but today it is commonly referred to as the Mie series, named after Gustav Mie from his work in [16]. Since then the topic has been studied extensively, and the results are summarized in many textbooks [2, 3, 14, 21, 27]. The Mie series is used in a wide variety of applications such as optics, climate modelling, astro physics, nano science and biomedical imaging [2, 10, 17, 24].

When the spherical scatterer is much smaller than the wavelength of the incident wave, the Rayleigh scattering approximation can be applied [28]. When the size of the scatterer exceeds about 10% of the wavelength of the incident wave, this approximation breaks down and the Mie series solution has to be applied. Since the advent of modern computers, much work has been done on implementing stable and reliable algorithms of Mie series calculations [5, 7, 9, 15, 23, 30]. This has resulted in efficient calculations of Mie series with size parameters on the order of 10 000. Some examples of scenarios that have been considered are: Spheres of different dielectric and magnetic materials, layered spheres, anisotropic spheres, distorted spheres and spheres in an absorbing medium [10]. Recently, a summarizing article was presented [24] where the history of the Mie series is presented in detail. Analytic expressions for scattering from a layered sphere and the numerical implementation of the problem was presented in [24]. The authors of this report were surprised to find no reference to prior work that considers the scattering from a layered sphere with an arbitrary number of layers, and with admittance sheets at the interfaces. This type of problem has much use in the analysis of electromagnetic absorbers, which commonly consists of single or multiple layers of dielectric or magnetic materials, resistive sheets and circuit analog structures [18].

Electromagnetic absorbers are commonly used to attenuate electromagnetic signals and reduce the reflection and transmission from particular objects. Examples of areas where absorbers are used are in free space measurement setups for electromagnetic characterization of antennas or other objects [29], and in defense applications such as radar cross section (RCS) reduction [13, 21]. Most absorbers are designed for a planar structure of infinite extent, while most real applications involve that the absorberis applied to a curved structure, such as the body of an aircraft. Surprisingly little work exists with respect to the degradation of the absorber performance due to curvature. In [4] a Luneberg-Kliene expansion of the scattered field from a cylinder and a sphere is carried out to identify a correction term proportional to the radius of curvature of the scatterer, and in [12] the performance degradation of a five layer Jaumann absorber applied to a cylinder is calculated. In [26] a series of different absorbers are evaluated when applied to a perfect electric conductor (PEC) cylinder, and a conclusion in this work is that by normalizing the monostatic scattering from a coated cylinder with either the scattering from the uncoated structure, or the scattering from an enclosing PEC structure, a comparison can be made to a corresponding planar absorber design.

In this work, the scattering from a multilayered sphere is calculated by expanding the electric and magnetic fields in spherical vector waves. The structure of the specific scattering problem implies that all information of the scattered fields are stored in the transition matrix (or T-matrix), the mapping matrix between the incident and scattered fields. Once this mapping has been determined, the scattered fields are easily calculated. In the special case of scattering of a linearly polarized plane wave from a layered sphere with isotropic materials the T-matrix is diagonal, which greatly simplifies the solution of calculating the scattered fields. We use the T-matrix to determine the monostatic RCS of a PEC sphere coated by different types of classical electromagnetic absorbers, such as the Salisbury screen [22], Jaumann absorber [12], Chambers-Tennant absorber [6], conductive dielectric absorber, thin magnetic absorber and different types of circuit analog absorbers (CAA). By utilizing the normalization scheme that was first presented in [26] the monostatic RCS of the coated spheres can be compared to the corresponding planar design of the absorber under test. This study gives information of the performance degradation of absorbers due to curvature, and it is observed that electromagnetic absorbers of the same type display similar behavior when exposed to curvature.

This report is organized as follows: In Section 2 the theory of spherical vector waves is presented and in Section 3 the theory of scattering from layered spheres with admittance sheets at the interfaces is presented. This content is based on the notation and approach used in [14], where scattering from a PEC sphere, dielectric sphere, and layered spheres without thin sheets at the interfaces are considered. A numerical implementation of the theory in Sections 2-3 is presented in Section 4. In Section 5 simulation results of the implementation in Section 4 are presented, where the monostatic RCS of different electromagnetic absorbers applied to a sphere is calculated, and some concluding remarks are presented in Section 6. In Appendix A a detailed analytic derivation is presented of the scattering from a layered sphere with admittance sheets at the interfaces, and in Appendix B the implemented code

is benchmarked against different commercial software.

2 Spherical vector waves

The theory and notation presented in this section is based on the work in [14]. The time convention $e^{j\omega t}$ is used throughout this report.

2.1 Expansion of fields

In order to construct an orthogonal set of spherical vector waves with the right properties one needs to introduce a vector valued version of the ordinary scalar spherical harmonics [14]

$$Y_{\sigma ml}(\theta, \phi) = \sqrt{\frac{\varepsilon_m}{2\pi}}\sqrt{\frac{2l+1}{2}\frac{(l-m)!}{(l+m)!}}P_l^m(\cos\theta)\begin{Bmatrix} \cos m\phi \\ \sin m\phi \end{Bmatrix} \tag{2.1}$$

where the Neumann factor ε_m is defined as

$$\varepsilon_m = 2 - \delta_{m0}, \quad \text{i.e. } \epsilon_0 = 1, \ \varepsilon_m = 2, \ m > 0. \tag{2.2}$$

The spherical vector harmonics are here denoted $\boldsymbol{A}_{\tau\sigma ml}(\hat{\boldsymbol{r}})$, where $\tau = 1, 2, 3$ is the spherical vector wave index, σ is the even/odd mode index, $m = 0, 1, 2, .., l-1, l$ is the azimuthal mode index, and $l = 0, 1, 2, ..., \infty$ is the spherical harmonics index. In order to simplify the notation, we introduce a multiindex $n = (\sigma, m, l)$ which results in the spherical vector harmonics being denoted $\boldsymbol{A}_{\tau n}(\hat{\boldsymbol{r}})$. The spherical vector harmonics are generated from the relations

$$\begin{cases} \boldsymbol{A}_{1n}(\hat{\boldsymbol{r}}) = \dfrac{1}{\sqrt{l(l+1)}}\nabla Y_n(\hat{\boldsymbol{r}}) \times \hat{\boldsymbol{r}} \\[2ex] \boldsymbol{A}_{2n}(\hat{\boldsymbol{r}}) = \dfrac{1}{\sqrt{l(l+1)}}r\nabla Y_n(\hat{\boldsymbol{r}}) \\[2ex] \boldsymbol{A}_{3n}(\hat{\boldsymbol{r}}) = \hat{\boldsymbol{r}}Y_n(\hat{\boldsymbol{r}}) \end{cases} \tag{2.3}$$

where $\boldsymbol{A}_{1n}$, $\boldsymbol{A}_{2n}$, and $\boldsymbol{A}_{3n}$ are orthogonal, and $\boldsymbol{A}_{1n}$ and $\boldsymbol{A}_{2n}$ are tangential to spherical surfaces. A far field vector can be expanded in spherical vector waves using the Fourier expansion

$$\boldsymbol{F}(\hat{\boldsymbol{r}}) = \sum_{\tau=1}^{3}\sum_{n=\sigma,m,l} a_{\tau n}\boldsymbol{A}_{\tau n}(\hat{\boldsymbol{r}}), \tag{2.4}$$

where the Fourier coefficients $a_{\tau n}$ are determined through the relation

$$a_{\tau n} = \int_{\Omega} \boldsymbol{F}(\hat{\boldsymbol{r}}) \cdot \boldsymbol{A}_{\tau n}(\hat{\boldsymbol{r}}) \, \mathrm{d}\Omega. \tag{2.5}$$

We are now ready to introduce the spherical vector waves used to describe the electric- and magnetic field on a spherical surface. The out-going spherical vector waves are given by

$$
\begin{cases}
\boldsymbol{u}_{1n}(k\boldsymbol{r}) = h_l^{(2)}(kr)\boldsymbol{A}_{1n}(\hat{\boldsymbol{r}}) \\[4mm]
\boldsymbol{u}_{2n}(k\boldsymbol{r}) = \dfrac{(krh_l^{(2)}(kr))'}{kr}\boldsymbol{A}_{2n}(\hat{\boldsymbol{r}}) + \sqrt{l(l+1)}\dfrac{h_l^{(2)}(kr)}{kr}\boldsymbol{A}_{3n}(\hat{\boldsymbol{r}}).
\end{cases}
\tag{2.6}
$$

and the regular spherical vector waves are

$$
\begin{cases}
\boldsymbol{v}_{1n}(k\boldsymbol{r}) = j_l(kr)\boldsymbol{A}_{1n}(\hat{\boldsymbol{r}}) \\[4mm]
\boldsymbol{v}_{2n}(k\boldsymbol{r}) = \dfrac{(krj_l(kr))'}{kr}\boldsymbol{A}_{2n}(\hat{\boldsymbol{r}}) + \sqrt{l(l+1)}\dfrac{j_l(kr)}{kr}\boldsymbol{A}_{3n}(\hat{\boldsymbol{r}}),
\end{cases}
\tag{2.7}
$$

where $j_l(kr)$ is the spherical Bessel function, $h_l^{(2)}(kr)$ is the spherical Hankel function, defined as $h_l^{(2)}(kr) = j_l(kr) - \mathrm{j}y_l(kr)$, and $y_l(ka)$ is the spherical Neumann function. We construct a sphere enclosing the scatterer and expand the total electric field outside the sphere as

$$
\boldsymbol{E}(\boldsymbol{r},\omega) = \boldsymbol{E}_{\mathrm{i}}(\boldsymbol{r},\omega) + \boldsymbol{E}_{\mathrm{s}}(\boldsymbol{r},\omega) = \sum_{\tau=1}^{3}\sum_{l=0}^{\infty}\sum_{m=0}^{l}\sum_{\sigma=\mathrm{e,o}} \left(a_{\tau\sigma ml}\boldsymbol{v}_{\tau\sigma ml}(k\boldsymbol{r}) + f_{\tau\sigma ml}\boldsymbol{u}_{\tau\sigma ml}(k\boldsymbol{r})\right)
$$

$$
= \sum_{\tau=1}^{3}\sum_{n} \left(a_{\tau n}\boldsymbol{v}_{\tau}(k\boldsymbol{r}) + f_{\tau n}\boldsymbol{u}_{\tau n}(k\boldsymbol{r})\right) \quad (2.8)
$$

where $a_{\tau n}$ are the incident field coefficients and $f_{\tau n}$ are the scattered field coefficients.

3 Sphere scattering

The theory and notation presented in this section is based on the work in [14]. The theoretical addition of this section in relation to [14] is the treatment of surface currents at the interfaces between the layers of the sphere in Section 3.5.

3.1 Solution method

To solve a Mie series scattering problem, we use the boundary conditions of the electric and magnetic fields at each side of an interface

$$
\hat{\boldsymbol{n}} \times (\boldsymbol{E}_2 - \boldsymbol{E}_1) = 0, \qquad \hat{\boldsymbol{n}} \times (\boldsymbol{H}_2 - \boldsymbol{H}_1) = \boldsymbol{J}_{\mathrm{S}} \tag{3.1}
$$

where $\boldsymbol{E}_1$, $\boldsymbol{H}_1$ are the fields in region 1, $\boldsymbol{E}_2$, $\boldsymbol{H}_2$ are the fields in region 2, $\boldsymbol{J}_{\mathrm{S}}$ is the surface current at the interface, and $\hat{\boldsymbol{n}}$ is the normal vector of the surface pointing from region 1 towards region 2. If the materials in the two regions are linear, a

linear mapping exists between the incident field coefficients $a_{\tau n}$ and the scattered field coefficients $f_{\tau n}$

$$f_{\tau n} = t_{\tau l} a_{\tau n}, \qquad \tau = 1, 2. \tag{3.2}$$

The mapping matrix between the incident and scattered field coefficients in (3.2) is called the transition matrix or the T-matrix, and its coefficients $t_{\tau l}$ are determined from the boundary conditions of the specific problem, as is shown in Sections 3.3–3.5. An incident, monochromatic, plane wave is represented in spherical vector waves as

$$\begin{cases} \boldsymbol{E}_{\mathrm{i}}(\boldsymbol{r}, \omega) = \boldsymbol{E}_0 \mathrm{e}^{-\mathrm{j}\hat{\boldsymbol{k}}_{\mathrm{i}} \cdot \boldsymbol{r}} = \displaystyle\sum_{\tau=1}^{2} \sum_{n} a_{\tau n} \boldsymbol{v}_{\tau n}(k\boldsymbol{r}) \\[2mm] \boldsymbol{H}_{\mathrm{i}}(\boldsymbol{r}, \omega) = \boldsymbol{H}_0 \mathrm{e}^{-\mathrm{j}\hat{\boldsymbol{k}}_{\mathrm{i}} \cdot \boldsymbol{r}} = \dfrac{\mathrm{j}}{\eta_0 \eta} \displaystyle\sum_{\tau=1}^{2} \sum_{n} a_{\tau n} \boldsymbol{v}_{\bar{\tau} n}(k\boldsymbol{r}) \end{cases} \tag{3.3}$$

where η_0, η are the free space and relative wave impedance. The expansion coefficients are

$$\begin{cases} a_{1n} = 4\pi(-\mathrm{j})^l \boldsymbol{E}_0 \cdot \boldsymbol{A}_{1n}(\hat{\boldsymbol{k}}_{\mathrm{i}}) \\ a_{2n} = 4\pi(-\mathrm{j})^{l-1} \boldsymbol{E}_0 \cdot \boldsymbol{A}_{2n}(\hat{\boldsymbol{k}}_{\mathrm{i}}) \\ a_{3n} = 4\pi(-\mathrm{j})^{l-1} \boldsymbol{E}_0 \cdot \boldsymbol{A}_{3n}(\hat{\boldsymbol{k}}_{\mathrm{i}}) = 0, \end{cases} \tag{3.4}$$

where since $a_{3n} = 0$ the $\tau = 3$ terms in (3.3) does not contribute and have been excluded. The dual index $\bar{\tau}$ is indicating that $\tau = 1 \to \bar{\tau} = 2$, and $\tau = 2 \to \bar{\tau} = 1$. If the plane wave is incident along the z-axis, i.e. $= \hat{\boldsymbol{k}}_{\mathrm{i}} = \hat{\boldsymbol{z}}$, the expansion coefficients are

$$\begin{cases} a_{1n} = (-\mathrm{j})^l \delta_{m1} \sqrt{2\pi(2l+1)} \boldsymbol{E}_0 \cdot (\delta_{\sigma\mathrm{o}}\hat{\boldsymbol{x}} - \delta_{\sigma\mathrm{e}}\hat{\boldsymbol{y}}) \\ a_{2n} = (-\mathrm{j})^{l-1} \delta_{m1} \sqrt{2\pi(2l+1)} \boldsymbol{E}_0 \cdot (\delta_{\sigma\mathrm{e}}\hat{\boldsymbol{x}} + \delta_{\sigma\mathrm{o}}\hat{\boldsymbol{y}}) \\ a_{3n} = 0, \end{cases} \tag{3.5}$$

where $\delta_{\sigma\mathrm{o}} = 1$ if $\sigma = \mathrm{o}$ and $\delta_{\sigma\mathrm{o}} = 0$ if $\sigma \neq \mathrm{o}$, and in the same manner $\delta_{m1} = 1$ if $m = 1$ and $\delta_{m1} = 0$ if $m \neq 1$. Using this representation of the incident field, the scattered field can be determined.

3.2 The scattering parameters

The scattering dyadic is given by

$$\mathbf{S}(\hat{\boldsymbol{r}}, \hat{\boldsymbol{k}}_{\mathrm{i}}) = -\frac{4\pi}{\mathrm{j}k} \sum_{nn'} \boldsymbol{a}_n^*(\hat{\boldsymbol{r}}) T_{nn'} \boldsymbol{a}_{n'}(\hat{\boldsymbol{r}}) \tag{3.6}$$

where in this context the multiindex $n = (\tau, \sigma, m, l)$ is used (as opposed to $n = (\sigma, m, l)$ which is used in the rest of the report), and where $T_{nn'}$ is the T-matrix defined as

$$f_n = \sum_{nn'} T_{nn'} a_{n'}, \tag{3.7}$$

and where the complex vector spherical harmonics $\boldsymbol{a}_n(\hat{\boldsymbol{r}})$ are defined as

$$\boldsymbol{a}_n(\hat{\boldsymbol{r}}) = \mathrm{j}^{\tau-l-1} \boldsymbol{A}_n(\hat{\boldsymbol{r}}), \tag{3.8}$$

with the parity condition $\boldsymbol{a}_n^*(\hat{\boldsymbol{r}}) = \boldsymbol{a}_n(-\hat{\boldsymbol{r}})$. From the T-matrix, and thus alternatively from the scattering matrix, specific scattering properties of an object can be calculated. For example, the differential cross section of a scatterer is defined as

$$\frac{\mathrm{d}\sigma}{\mathrm{d}\Omega}(\hat{\boldsymbol{r}}, \hat{\boldsymbol{k}}_{\mathrm{i}}) = \frac{|\boldsymbol{F}(\hat{\boldsymbol{r}})|^2}{k^2|\boldsymbol{E}_0|^2} = 4\pi|\mathbf{S}(\hat{\boldsymbol{r}}, \hat{\boldsymbol{k}}_{\mathrm{i}}) \cdot \hat{\boldsymbol{p}}_{\mathrm{e}}|^2, \tag{3.9}$$

where $\hat{\boldsymbol{p}}_{\mathrm{e}} = \boldsymbol{E}_0/|\boldsymbol{E}_0|$, $\boldsymbol{E}_0$ is the incident field, and $\boldsymbol{F}(\hat{\boldsymbol{r}})$ is the scattered farfield. From the differential cross section, the scattering cross section is defined as

$$\sigma_{\mathrm{s}} = \frac{1}{4\pi} \int \frac{\mathrm{d}\sigma}{\mathrm{d}\Omega}(\hat{\boldsymbol{r}}, \hat{\boldsymbol{k}}_{\mathrm{i}}) \, \mathrm{d}\Omega = \sum_{nn'n''} b_{n''}^*(\hat{\boldsymbol{k}}_{\mathrm{i}}) T_{n''n}^\dagger T_{nn'} b_{n'}(\hat{\boldsymbol{k}}_{\mathrm{i}}) \tag{3.10}$$

where $b_n(\hat{\boldsymbol{k}}_{\mathrm{i}}) = -\mathrm{j}4\pi\boldsymbol{a}_n(\hat{\boldsymbol{k}}_{\mathrm{i}}) \cdot \hat{\boldsymbol{p}}_{\mathrm{e}}$, and from the scattering cross section, σ_{s}, the total cross section of a scatterer is defined as

$$\sigma_{\mathrm{t}} = \sigma_{\mathrm{s}} + \sigma_{\mathrm{a}}, \tag{3.11}$$

where σ_{a} is the absorption cross section of the scatterer. In this work, we are especially interested in the monostatic scattering properties of the object under study. The scattering dyadic in the backscattering direction, $\hat{\boldsymbol{r}} = -\hat{\boldsymbol{k}}_{\mathrm{i}}$, is

$$\mathbf{S}(-\hat{\boldsymbol{k}}_{\mathrm{i}}, \hat{\boldsymbol{k}}_{\mathrm{i}}) = -\frac{4\pi}{\mathrm{j}k} \sum_{nn'} \boldsymbol{a}_n^*(\hat{\boldsymbol{k}}_{\mathrm{i}}) T_{nn'} \boldsymbol{a}_{n'}(\hat{\boldsymbol{k}}_{\mathrm{i}}), \tag{3.12}$$

and the differential cross section is

$$\frac{\mathrm{d}\sigma}{\mathrm{d}\Omega}(-\hat{\boldsymbol{k}}_{\mathrm{i}}, \hat{\boldsymbol{k}}_{\mathrm{i}}) = \frac{64\pi^3}{k^2} \left| \sum_{nn'} \boldsymbol{a}_n(\hat{\boldsymbol{k}}_{\mathrm{i}}) T_{nn'} \boldsymbol{a}_{n'}(\hat{\boldsymbol{k}}_{\mathrm{i}}) \cdot \hat{\boldsymbol{p}}_{\mathrm{e}} \right|^2. \tag{3.13}$$

For a spherical scatterer, the T-matrix is diagonal with respect to all indices $n = (\tau, \sigma, m, l)$, and (3.10) simplifies to

$$\sigma_{\mathrm{s}} = \frac{2\pi}{k^2} \sum_{l=1}^{\infty}(2l + 1)(|t_{1l}|^2 + |t_{2l}|^2), \tag{3.14}$$

the scattered farfield $\boldsymbol{F}(\hat{\boldsymbol{r}})$ is in this case given by

$$\boldsymbol{F}(\hat{\boldsymbol{r}}) = \sum_{\tau=1}^{2} \sum_{n} \mathrm{j}^{\tau-l-1} f_{\tau n} \boldsymbol{A}_{\tau n}(\hat{\boldsymbol{r}}), \tag{3.15}$$

and the monostatic RCS of a spherical scatterer simplifies from (3.13) to

$$\frac{\mathrm{d}\sigma}{\mathrm{d}\Omega}(-\hat{\boldsymbol{k}}_{\mathrm{i}}, \hat{\boldsymbol{k}}_{\mathrm{i}}) = \frac{\pi}{k^2} \left| \sum_{l=1}^{\infty}(-1)^l(2l + 1)(t_{1l} - t_{2l}) \right|^2 \tag{3.16}$$

which is the main scattering quantity of interest in this work.

3.3 Scattering from a perfectly conducting sphere

The most simple case of Mie scattering is the scattering from a PEC sphere, see Figure 1. The total electric field outside of the scatterer is expanded in the regular and out-going spherical vector waves as in (2.8), where the coefficients of the incident plane wave $a_{\tau n}$ are known, see (3.5), and the coefficients of the scattered field $f_{\tau n}$ are unknown.
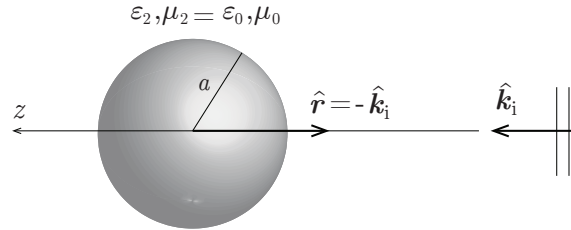

Figure 1: Electromagnetic scattering of a plane wave from a PEC sphere with radius a. In this work the main focus is on finding the monostatic scattering, which corresponds to $\hat{\boldsymbol{r}} = -\hat{\boldsymbol{k}}_{\mathrm{i}}$.

This field representation is inserted into the boundary conditions in (3.1) where inside the conducting sphere the electric field is zero, resulting in the relations

$$\begin{cases} a_{1n}j_l(ka) + f_{1n}h_l^{(2)}(ka) = 0 \\ a_{2n}(kaj_l(ka))' + f_{1n}(kah_l^{(2)}(ka))' = 0, \end{cases} \tag{3.17}$$

where a is the radius of the scatterer. The expression (3.17) can be rewritten as

$$f_{\tau n} = t_{\tau l}a_{\tau n}, \qquad \tau = 1, 2 \tag{3.18}$$

which is a linear mapping between $a_{\tau n}$ and $f_{\tau n}$, where

$$t_{1l} = -\frac{j_l(ka)}{h_l^{(2)}(ka)}, \qquad t_{2l} = -\frac{(kaj_l(ka))'}{(kah_l^{(2)}(ka))'}. \tag{3.19}$$

From the T-matrix elements in (3.19) the scattered monostatic RCS is given by the expression in (3.16). The scattered electric field outside of the scatterer is given by

$$\boldsymbol{E}_{\mathrm{s}}(\boldsymbol{r},\omega) = \sum_{\tau=1}^{2}\sum_{n} f_{\tau n}\boldsymbol{u}_{\tau n}(k\boldsymbol{r}). \tag{3.20}$$

3.4 Scattering from a dielectric sphere

The scattering from a dielectric sphere is calculated using the same approach as for the PEC sphere, the main difference being that in this case the continuity of both the electric and magnetic fields at the surface of the scatterer are utilized in the calculation of the scattered field coefficients, see Figure 2. As in Section 3.3, the
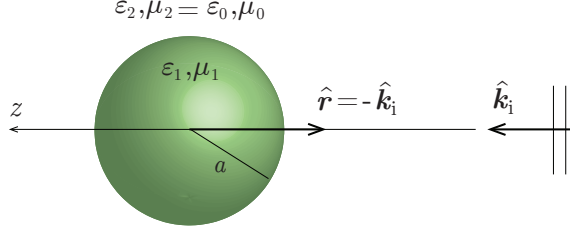
Figure 2: Electromagnetic scattering of a plane wave from a dielectric sphere with radius a.

incident field is given by

$$\boldsymbol{E}_{\mathrm{i}}(\boldsymbol{r},\omega) = \boldsymbol{E}_0 \mathrm{e}^{-\mathrm{j}kz} = \sum_{\tau=1}^{2}\sum_{n} a_{\tau n}\boldsymbol{v}_{\tau n}(k\boldsymbol{r}) \qquad (3.21)$$

where the coefficients $a_{\tau n}$ for a plane wave, incident in the z-direction, are given in (3.5) as

$$\begin{cases} a_{1n} = (-\mathrm{j})^l\sqrt{2\pi(2l+1)}\boldsymbol{E}_0 \cdot (\delta_{\sigma\mathrm{o}}\hat{\boldsymbol{x}} - \delta_{\sigma\mathrm{e}}\hat{\boldsymbol{y}}) \\ a_{2n} = -(-\mathrm{j})^{l+1}\sqrt{2\pi(2l+1)}\boldsymbol{E}_0 \cdot (\delta_{\sigma\mathrm{e}}\hat{\boldsymbol{x}} + \delta_{\sigma\mathrm{o}}\hat{\boldsymbol{y}}) \\ a_{3n} = 0. \end{cases}$$

The unknown scattered field is given by

$$\boldsymbol{E}_{\mathrm{s}}(\boldsymbol{r},\omega) = \sum_{\tau=1}^{2}\sum_{n} f_{\tau n}\boldsymbol{u}_{\tau n}(k\boldsymbol{r}), \quad r > a, \qquad (3.22)$$

and the total fields outside the scatterer are

$$\begin{cases} \boldsymbol{E}(\boldsymbol{r},\omega) = \sum_{\tau=1}^{2}\sum_{n}(a_{\tau n}\boldsymbol{v}_{\tau n}(k\boldsymbol{r}) + f_{\tau n}\boldsymbol{u}_{\tau n}(k\boldsymbol{r})) \\ \boldsymbol{H}(\boldsymbol{r},\omega) = \dfrac{\mathrm{j}}{\eta_0\eta}\sum_{\tau=1}^{2}\sum_{n}(a_{\tau n}\boldsymbol{v}_{\bar{\tau}n}(k\boldsymbol{r}) + f_{\tau n}\boldsymbol{u}_{\bar{\tau}n}(k\boldsymbol{r})) \end{cases} \qquad (3.23)$$

while the total fields inside the scatterer, which we denote $\boldsymbol{E}_1$ and $\boldsymbol{H}_1$, are

$$\begin{cases} \boldsymbol{E}_1(\boldsymbol{r},\omega) = \sum_{\tau=1}^{2}\sum_{n}\alpha_{\tau n}\boldsymbol{v}_{\tau n}(k_1\boldsymbol{r}) \\ \boldsymbol{H}_1(\boldsymbol{r},\omega) = \dfrac{\mathrm{j}}{\eta_0\eta_1}\sum_{\tau=1}^{2}\sum_{n}\alpha_{\tau n}\boldsymbol{v}_{\bar{\tau}n}(k_1\boldsymbol{r}). \end{cases} \qquad (3.24)$$

The boundary conditions at the surface of the sphere are

$$\begin{cases} \hat{\boldsymbol{r}} \times \boldsymbol{E}_1(\boldsymbol{r},\omega)|_{r=a} = \hat{\boldsymbol{r}} \times \boldsymbol{E}_2(\boldsymbol{r},\omega)|_{r=a} \\ \hat{\boldsymbol{r}} \times \boldsymbol{H}_1(\boldsymbol{r},\omega)|_{r=a} = \hat{\boldsymbol{r}} \times \boldsymbol{H}_2(\boldsymbol{r},\omega)|_{r=a} \end{cases} \qquad (3.25)$$

which result in the system of equations

$$
\begin{cases}
\alpha_{1n}j_l(k_1a) = a_{1n}j_l(ka) + f_{1n}h_l^{(2)}(ka) \\[2mm]
\alpha_{2n}\dfrac{(k_1aj_l(k_1a))'}{k_1a} = a_{2n}\dfrac{(kaj_l(ka))'}{ka} + f_{2n}\dfrac{(kah_l^{(2)}(ka))'}{ka} \\[2mm]
\dfrac{1}{\eta_1}\alpha_{1n}\dfrac{(k_1aj_l(k_1a))'}{k_1a} = \dfrac{1}{\eta}\left(a_{1n}\dfrac{(kaj_l(ka))'}{ka} + f_{1n}\dfrac{(kah_l^{(2)}(ka))'}{ka}\right) \\[2mm]
\dfrac{1}{\eta_1}\alpha_{2n}j_l(k_1a) = \dfrac{1}{\eta}\left(a_{2n}j_l(k_1a) + f_{2n}h_l^{(2)}(ka)\right).
\end{cases}
\tag{3.26}
$$

The expression (3.26) can be written as a T-matrix relation

$$
f_{\tau l} = t_{\tau l}a_{\tau n} = \begin{pmatrix} t_{1l} & 0 \\ 0 & t_{2l} \end{pmatrix}\begin{pmatrix} a_{1n} \\ a_{2n} \end{pmatrix}.
\tag{3.27}
$$

If the terms in (3.26) are rearranged, and the coefficients $\alpha_{\tau n}$ are eliminated, the final expression of the T-matrix elements is

$$
t_{\tau l} = \frac{j_l(ka)(k_1aj_l(k_1a))' - \gamma_\tau j_l(ka)(kaj_l(ka))'}{h_l^{(2)}(ka)(k_1aj_l(k_1a))' - \gamma_\tau j_l(k_1a)(kaj_l(ka))'}
\tag{3.28}
$$

where $\gamma_\tau = \delta_{\tau 1}(\mu_1/\mu) + \delta_{\tau 2}(\epsilon_1/\epsilon)$, and where ϵ_1, ϵ, μ_1, μ are the relative permittivity and permeability of the scatterer and the surrounding medium, respectively. The result (3.28) implies that the scattered field looks as if it comes from an electric multipole ($\tau = 1$), and a magnetic multipole ($\tau = 2$).

3.5   Scattering from layered spheres with resistive sheets

We are now ready to treat the more general scattering case of multilayered spheres with resistive sheets at the interfaces, such as the structure in Figure 3. Let $r_1 \le r_2 \le \ldots \le r_N$ be the radii of the N layers of the sphere, and let ϵ_i and μ_i, $i = 1, 2, \ldots, N$ be the (relative) permittivity and permeability, respectively, of the layers. The outmost radius is r_N, and outside this sphere we have free space, $i.e.$ $\epsilon_{N+1} = \epsilon_0$ and $\mu_{N+1} = \mu_0$. The total fields in each region are given by

$$
\begin{cases}
\boldsymbol{E}^{(i)}(\boldsymbol{r}, \omega) = \displaystyle\sum_{\tau=1}^{2}\sum_{n} A_{\tau n}^{(i)}(\boldsymbol{v}_{\tau n}(k_i\boldsymbol{r}) + t_{\tau n}^{(i-1)}\boldsymbol{u}_{\tau n}(k_i\boldsymbol{r})) \\[3mm]
\boldsymbol{H}^{(i)}(\boldsymbol{r}, \omega) = \dfrac{\mathrm{j}}{\eta_0\eta_i}\displaystyle\sum_{\tau=1}^{2}\sum_{n} A_{\tau n}^{(i)}(\boldsymbol{v}_{\bar\tau n}(k_i\boldsymbol{r}) + t_{\tau n}^{(i-1)}\boldsymbol{u}_{\bar\tau n}(k_i\boldsymbol{r}))
\end{cases}
\quad r_{i-1} < r < r_i
\tag{3.29}
$$

where $i = 1, 2, \ldots, N + 1$ correspond to each region in space, N is the number of layers of the scatterer, $k_i = k_0\sqrt{\epsilon_i\mu_i}$, $\eta_i = \sqrt{\mu_i/\epsilon_i}$, $\eta_{N+1} = \sqrt{\mu_0/\epsilon_0}$, and $t_{\tau l}^{(i)}$ are the unknowns. We define $t_{\tau l}^{(0)} = 0$ since $\boldsymbol{E}^{(0)}(\boldsymbol{r}, \omega)$ is non-singular at $r_0 = 0$. The boundary conditions at the interfaces are in this case

$$
\begin{cases}
\hat{\boldsymbol{n}} \times \boldsymbol{E}^{(i)}(\boldsymbol{r}, \omega)|_{r=a_i} = \hat{\boldsymbol{n}} \times \boldsymbol{E}^{(i+1)}(\boldsymbol{r}, \omega)|_{r=a_i} \\[2mm]
\hat{\boldsymbol{n}} \times \boldsymbol{H}^{(i)}(\boldsymbol{r}, \omega)|_{r=a_i} - \hat{\boldsymbol{n}} \times \boldsymbol{H}^{(i+1)}(\boldsymbol{r}, \omega)|_{r=a_i} = \boldsymbol{J}_{\mathrm{S}}^{(i)}(\boldsymbol{r}, \omega)|_{r=a_i}
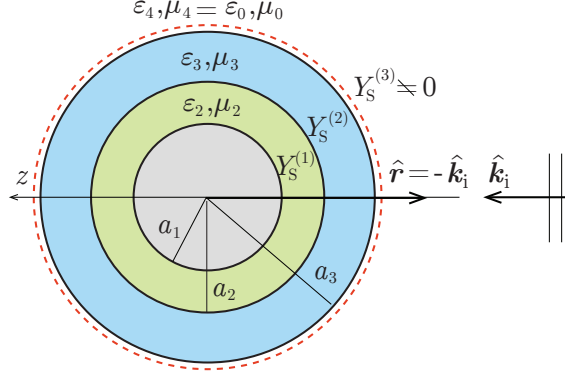\end{cases}
\tag{3.30}
$$

Figure 3: Electromagnetic scattering from a layered sphere with a PEC core and possibly with admittance sheets at the interfaces. In this example, a PEC sphere with radius a_1 is coated with two dielectric/magnetic layers with thicknesses $a_2 - a_1$, $a_3 - a_2$, and an infinitely thin admittance sheet $Y_{\mathrm{S}}^{(3)}$ is located at the outer boundary.

where $\boldsymbol{J}_{\mathrm{S}}^{(i)} = Y_{\mathrm{S}}^{(i)}\hat{\boldsymbol{n}}\times(\boldsymbol{E}^{(i)}\times\hat{\boldsymbol{n}})|_{r=a_i} = Y_{\mathrm{S}}^{(i)}\hat{\boldsymbol{n}}\times(\boldsymbol{E}^{(i+1)}\times\hat{\boldsymbol{n}})|_{r=a_i}$. In the same manner as in Section 3.4, the boundary conditions (3.30) result in a system of equations for each interface of the layered sphere. The solution to this system is found by first finding the T-matrix elements of the innermost interface, and then iterating through each interface of the layered sphere. This results in a recursion relation of the T-matrix elements, see Appendix 6 for a detailed derivation, in form of a Möbius transform

$$t_{\tau l}^{(i)} = -\frac{a_\tau^{(i)} t_{\tau l}^{(i-1)} + b_\tau^{(i)}}{c_\tau^{(i)} t_{\tau l}^{(i-1)} + d_\tau^{(i)}}. \tag{3.31}$$

To simplify the expressions of the coefficients in (3.31), we introduce the Riccati-Bessel functions and their derivatives [1, 19]

$$
\begin{aligned}
\psi_l(z) &= z j_l(z), & \xi_l(z) &= z h_l^{(2)}(z) \\
\psi_l'(z) &= j_l(z) + z j_l'(z), & \xi_l'(z) &= h_l^{(2)}(z) + z h_l'^{(2)}(z).
\end{aligned}
\tag{3.32}
$$

For $\tau = 1$ the coefficients are

$$
\begin{cases}
a_1^{(i)} = \dfrac{\eta_i}{\eta_{i+1}}\xi_l(k_i r_i)\psi_l'(k_{i+1}r_i) - \xi_l'(k_i r_i)\psi_l(k_{i+1}r_i) - \mathrm{j}\eta_i Y_{\mathrm{S}}^{(i)}\xi_l(k_i r_i)\psi_l(k_{i+1}r_i) \\[2ex]
b_1^{(i)} = \dfrac{\eta_i}{\eta_{i+1}}\psi_l(k_i r_i)\psi_l'(k_{i+1}r_i) - \psi_l'(k_i r_i)\psi_l(k_{i+1}r_i) - \mathrm{j}\eta_i Y_{\mathrm{S}}^{(i)}\psi_l(k_i r_i)\psi_l(k_{i+1}r_i) \\[2ex]
c_1^{(i)} = \dfrac{\eta_i}{\eta_{i+1}}\xi_l(k_i r_i)\xi_l'(k_{i+1}r_i) - \xi_l'(k_i r_i)\xi_l(k_{i+1}r_i) - \mathrm{j}\eta_i Y_{\mathrm{S}}^{(i)}\xi_l(k_i r_i)\xi_l(k_{i+1}r_i) \\[2ex]
d_1^{(i)} = \dfrac{\eta_i}{\eta_{i+1}}\psi_l(k_i r_i)\xi_l'(k_{i+1}r_i) - \psi_l'(k_i r_i)\xi_l(k_{i+1}r_i) - \mathrm{j}\eta_i Y_{\mathrm{S}}^{(i)}\psi_l(k_i r_i)\xi_l(k_{i+1}r_i),
\end{cases}
\tag{3.33}
$$

and for $\tau = 2$ the coefficients are   3.33

$$
\begin{cases}
a_2^{(i)} = \dfrac{\eta_{i+1}}{\eta_i}\xi_l(k_i r_i)\psi_l'(k_{i+1}r_i) - \xi_l'(k_i r_i)\psi_l(k_{i+1}r_i) - \mathrm{j}\eta_{i+1}Y_{\mathrm{S}}^{(i)}\xi_l'(k_i r_i)\psi_l'(k_{i+1}r_i) \\[2mm]
b_2^{(i)} = \dfrac{\eta_{i+1}}{\eta_i}\psi_l(k_i r_i)\psi_l'(k_{i+1}r_i) - \psi_l'(k_i r_i)\psi_l(k_{i+1}r_i) - \mathrm{j}\eta_{i+1}Y_{\mathrm{S}}^{(i)}\psi_l'(k_i r_i)\psi_l'(k_{i+1}r_i) \\[2mm]
c_2^{(i)} = \dfrac{\eta_{i+1}}{\eta_i}\xi_l(k_i r_i)\xi_l'(k_{i+1}r_i) - \xi_l'(k_i r_i)\xi_l(k_{i+1}r_i) - \mathrm{j}\eta_{i+1}Y_{\mathrm{S}}^{(i)}\xi_l'(k_i r_i)\xi_l'(k_{i+1}r_i) \\[2mm]
d_2^{(i)} = \dfrac{\eta_{i+1}}{\eta_i}\psi_l(k_i r_i)\xi_l'(k_{i+1}r_i) - \psi_l'(k_i r_i)\xi_l(k_{i+1}r_i) - \mathrm{j}\eta_{i+1}Y_{\mathrm{S}}^{(i)}\psi_l'(k_i r_i)\xi_l'(k_{i+1}r_i).
\end{cases}
$$

$$(3.34)$$

It can be seen that the expressions in (3.33)–(3.34) reduce to the same recursive relations presented in [14, Ch. 8] if no surface currents are present at the interfaces. If a general homogeneous material is located at the center of the scatterer, the iteration starts by $i = 1$. However, If the innermost layer is a PEC then the iteration starts at $i = 2$, and it is initialized by

$$
t_{1l}^{(1)} = \frac{\psi_l(k_2 r_1)}{\xi_l(k_2 r_1)}, \qquad t_{2l}^{(1)} = \frac{\psi_l'(k_2 r_1)}{\xi_l'(k_2 r_1)}. \tag{3.35}
$$

4   Numerical implementation

4.1   Python code

The theory described in Sections 2-3 was implemented in Python as a function that calculates the scattered fields of a multilayer sphere with N layers of dielectric/magnetic materials, possibly with resistive sheets at the interfaces. The input parameters to the code are:

$$\texttt{material} = [[\epsilon_1, \mu_1], [\epsilon_2, \mu_2], ..., [\epsilon_{N+1}, \mu_{N+1}]], \qquad \texttt{d} = [d_1, d_2, ..., d_{N+1}]$$
$$\texttt{adm} = [Y_{\mathrm{S}1}, Y_{\mathrm{S}2}, ..., Y_{\mathrm{S}N+1}] \qquad\qquad \texttt{f} = \mathrm{linspace}(f_1, f_2, N_{\mathrm{f}})$$

where $\texttt{material}$ is an array consisting of $N + 1$ vectors containing the material parameters of the layered sphere, the material parameters of the medium at the center (which in this work is replaced by PEC boundary conditions) are $[\epsilon_1, \mu_1]$, and $[\epsilon_{N+1}, \mu_{N+1}]$ are the material parameters of the surrounding medium. The thickness of each layer is defined by the vector $\texttt{d}$ and the surface admittance at each interface is given by the vector $\texttt{adm}$. The code was also specifically modified to treat dispersive materials and reactive surfaces, such as capacitive and/or inductive sheets, using extended input arguments for each frequency:

$$\texttt{Material} = [\texttt{material}(f_1), \texttt{material}(f_2), ..., \texttt{material}(f_{N_f})]$$
$$\texttt{Adm} = [\texttt{adm}(f_1), \texttt{adm}(f_2), ..., \texttt{adm}(f_{N_f})]$$

where the parameters $\texttt{adm}$ and $\texttt{material}$ are defined as in the previous, non-dispersive case.

The numerical implementation is organized as follows: The spherical Bessel and Hankel functions are imported from standard packages in Python. The $\texttt{mathcal}$

package is used for higher accuracy (float precision of the special functions). A function called `Mobius()` is defined that takes the input parameters listed above, uses the expressions (3.31)-(3.34) to iterate through the T-matrix coefficients from the center layer outwards one layer at a time, and returns the T-matrix coefficients of the outermost layer of the scatterer. When these T-matrix coefficients have been extracted, all scattering information of the layered sphere can be calculated from the relations presented in Section 3.2, such as the scattering cross section, the extinction cross section and the monostatic cross section.

The numerical implementation was verified through a number of benchmarking simulations in Comsol Multiphysics, Computer Simulation Technology Microwave Studio (CST-MWS), and FEKO. The results, presented in Appendix 6, indicate good agreement between the code and the full wave simulation software. It was concluded that the Method of Moments (MoM) solver in CST-MWS is not capable of treating dielectric materials, and the finite element solvers of Comsol Multiphysics and CST-MWS are not well suited for scattering simulations of object larger than a few wavelengths in size due to high memory requirements. Due to the aforementioned reasons, out of the three software FEKO seems to be the best suited for RCS simulations of three dimensional structures larger than a few wavelengths in size, with lossy dielectric/magnetic materials and resistive sheets.

Emphasis is put on the truncation of the l-index in the numerical implementation. An expression for this truncation was presented by Wiscombe in [30] to achieve convergence on the order of 10^{-14} for the sum of the squared Mie scattering coefficients. It states that

$$l_{\max} = \begin{cases} x + 4x^{1/3} + 1, & 0.02 \leq x \leq 8 \\ x + 4.05x^{1/3} + 2, & 8 < x < 4200 \\ x + 4x^{1/3} + 2, & 4200 < x < 20000 \end{cases} \tag{4.1}$$

where $x = ka$ is the electric size of the scatterer. This truncation relation has been used for all scatterers under study in this work.

5 Absorbers on doubly curved surfaces

5.1 RCS simulations and normalizations

The expressions (3.31)-(3.34) are used specifically to evaluate the monostatic RCS from a PEC sphere coated by different types of electromagnetic absorbers, as in Figure 4. The absorbers under study consist of multiple layers of homogeneous, isotropic, dielectric and/or magnetic materials with or without losses and dispersion. Resistive sheets and frequency selective structures at the interfaces are treated, using equivalent circuit parameters, as a surface admittance, which can also be frequency dependent, see Figure 4. Three different simulations were carried out for each absorber scenario:

1. Scattering from a PEC sphere.

2. Scattering from a PEC sphere coated with an absorber.

3. Scattering from a PEC sphere enclosing the coated structure,

see Figure 5. The two PEC simulations were then used to normalize the absorber RCS, and then make a comparison between the performance of the curved absorber and a corresponding planar design.
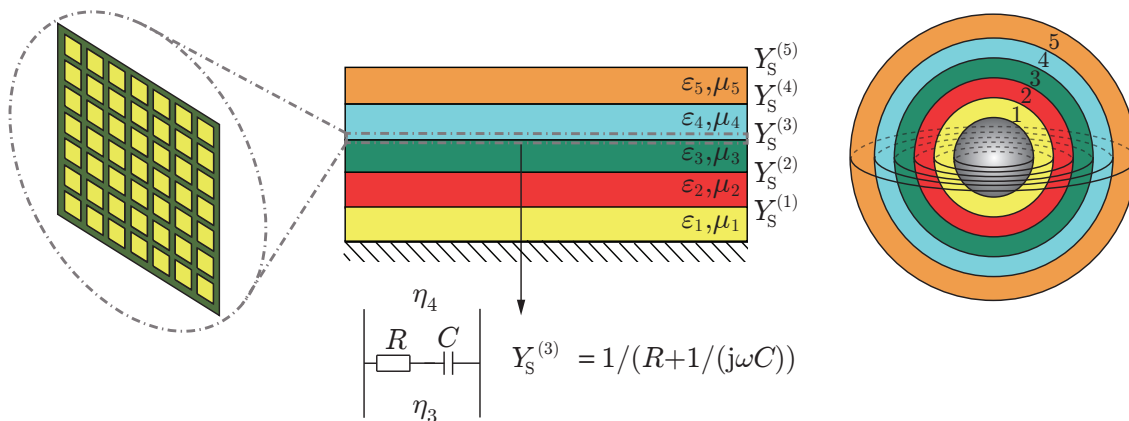

Figure 4: A planar multilayer absorber above a ground plane, consisting of different materials in the layers and possibly with admittance sheets $Y_S^{(i)}$ at the interfaces is presented in the middle. An example of a surface admittance consisting of a lattice of resistive patches is presented to the left, and to the right a multilayer sphere corresponding to the planar structure is presented.
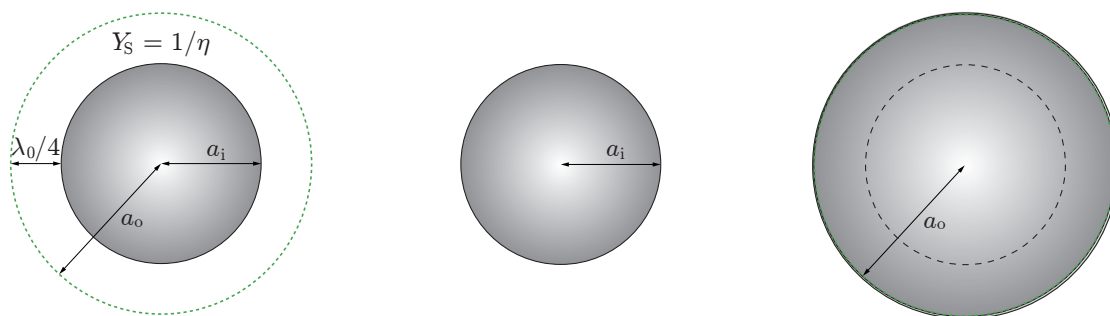
Figure 5: A PEC sphere with a coating Salisbury screen matched to the free space impedance (left), and the two normalization cases: A PEC sphere with the center radius a_i (center), an enclosing PEC sphere with the outer radius a_o (right).

5.2 Salisbury Screen

The first absorber under test is a classical Salisbury screen [22] consisting of a resistive sheet placed quarter of a wavelength, at the design frequency, from a ground

plane. For the best possible performance the impedance of the resistive sheet should be matched to the free space impedance, i.e. $Y_S = 1/\eta$, where $\eta = 377\ \Omega$. The three scenarios that are evaluated are presented in Figure 5, namely a PEC sphere coated by a resistive sheet, the same sphere without the absorber, and a PEC sphere enclosing the inner sphere and the absorber.

The monostatic RCS of a PEC sphere with radius a_o is presented to the left in Figure 6, and the monostatic RCS of a PEC sphere with radius a_i with a Salisbury screen is presented to the right in Figure 6, where all results are normalized with the cross section area of the scatterer. The radius of the PEC core was varied, both in the scenario with and without the Salisbury screen, corresponding to the different curves in Figure 6. It can be seen that the normalized monostatic RCS of a PEC sphere goes to 0 dB for higher frequencies, which is a familiar result. When comparing the two graphs in Figure 6 it can be seen that the Salisbury absorber reduces the RCS of the PEC sphere. However, in order to properly evaluate the performance of the spherical absorber, the RCS from the PEC sphere with a coating absorber is henceforth normalized according to the theory presented in Section 5.1. Normalized scattering data of the spherical Salisbury screen is presented in Figure 7, where the left plot is normalized with the RCS of the uncoated PEC scatterer, and the right plot is normalized with the RCS of an enclosing PEC. The colored curves correspond to different radii of the uncoated PEC scatterer, where in the plots labeled "inner radius" $k_0 a = 2\pi(a_i/\lambda_0)$ indicate the size of the uncoated structure with respect to the center wavelength of the absorber, and in the plots labeled "outer radius" $k_0 a = 2\pi(a_o/\lambda_0)$ indicate the size of the enclosing structure. This implies that all pairs of graphs of RCS data presented, using the two different normalizations, have been evaluated using the same size of scatterers corresponding to each color of the curves in the two graphs.
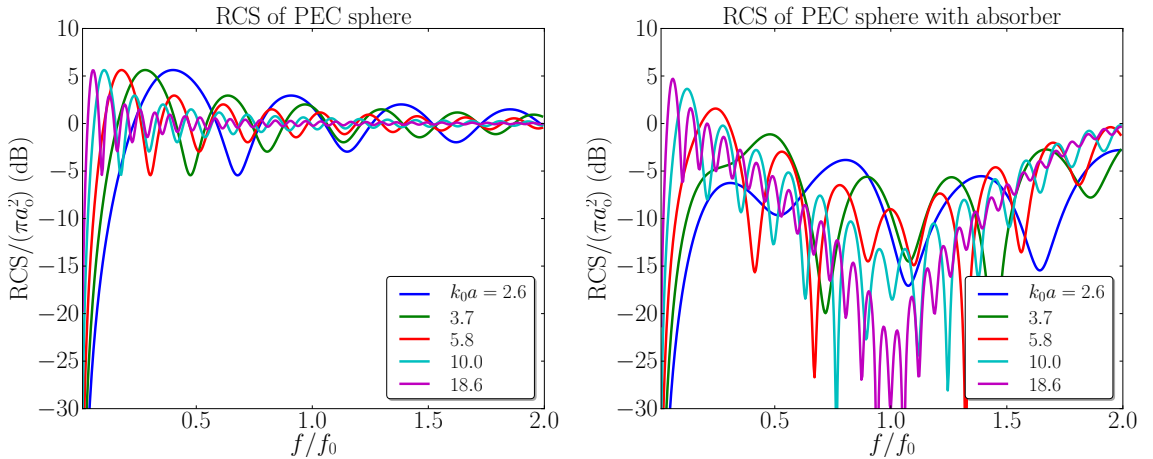

Figure 6: Monostatic RCS from a PEC sphere with a Salisbury screen (right) and the monostatic RCS from a PEC sphere (left).

In Figure 7 it can be seen that the absorber performance converges towards the planar result, indicated by the black curve, for large enough scatterers ($k_0 a \approx$

17). There is no significant difference between the results with the two different normalizations in Figure 7.
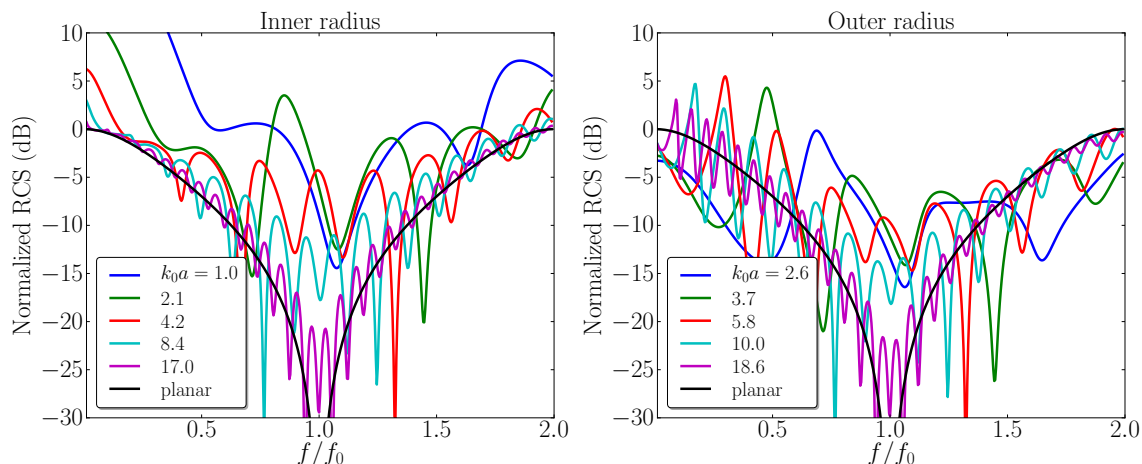

Figure 7: Monostatic RCS from a PEC sphere with a Salisbury screen, to the left normalized with the RCS of the inner PEC scatterer, and to the right normalized with the RCS of an enclosing PEC scatterer.

5.3   Jaumann absorber

The next absorber under study is a multilayered version of the salisbury screen, commonly referred to as a Jaumann absorber, see Figure 8. The speciffic design of the implemented absorber was presented in [12], where the performance degradation of Jaumann absorbers when applied to a cylinder is studied. This structure consists of five layers of resistive sheets with successively increasing admittance, seen from the incident wave, $Y_S^{(5)} = 1/1885$, $Y_S^{(4)} = 1/1205$, $Y_S^{(3)} = 1/679$, $Y_S^{(2)} = 1/302.1$, $Y_S^{(1)} = 1/71.40$ $[\Omega^{-1}]$, with the distance $d = \lambda_0/4$ between the sheets, and a spacer material with relative permittivity $\epsilon_r = 1.035$. The results in Figures 9-10 indicate that the
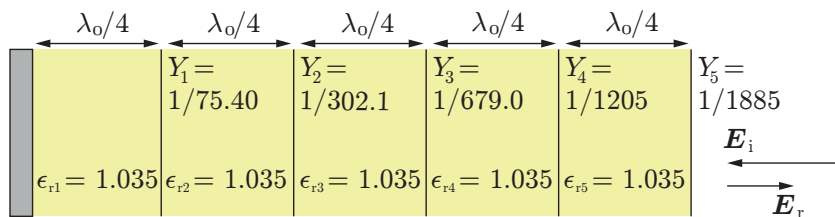

Figure 8: Jaumann absorber consisting of five resistive sheets with tuned impedances.

performance of this type of absorber also converges towards the planar curve, but at a slower rate than the single layer Salisbury screen. Also, the results for large scatterers seem to oscillate with the mean value given by the planar curve. This is most likely due to a surface wave at the center of the structure. A significant difference

can be noticed between the results being normalized with respect to the inner, uncoated, scatterer, and the data that is normalized with respect to an enclosing PEC sphere. The curves in Figure 9 indicate that, for thick absorbing structures, the normalization with respect to the enclosing PEC structure might overestimate the performance of the absorber.
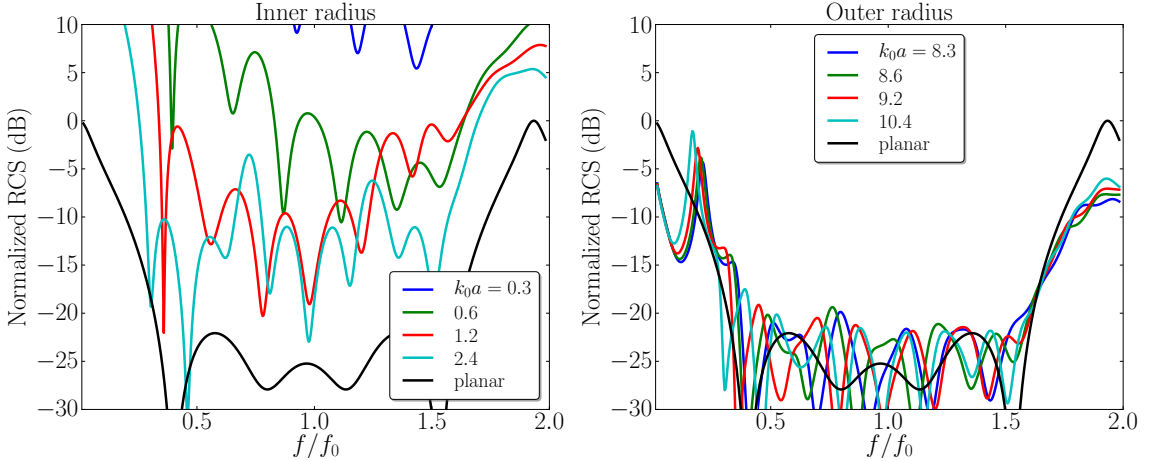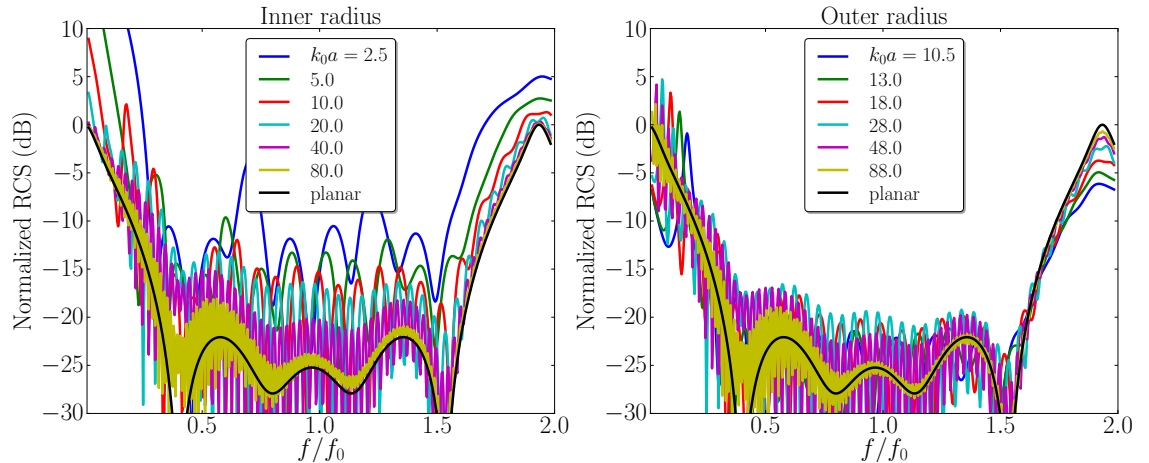

Figure 9: Monostatic RCS from a PEC sphere with a Jaumann absorber, to the left normalized with the RCS of the inner PEC scatterer, and to the right normalized with the RCS of an enclosing PEC scatterer.

Figure 10: Monostatic RCS from a PEC sphere with a Jaumann absorber, to the left normalized with the RCS of the inner PEC scatterer, and to the right normalized with the RCS of an enclosing PEC scatterer.

5.4 Capacitive Salisbury screen

For practical reasons it is commonly desirable to design absorbers with as small thickness as possible, while not significantly reducing the bandwidth of the absorber. In [20] it is shown that the maximum bandwidth B of an absorber backed by a PEC

ground plane is bounded by the thickness of the structure d, where a thinner absorber implies lower maximum bandwidth. One way to achieve B/d close to this physical limit is to add capacitive sheets to the absorber. In [11] a thin, ultra-wideband absorber based on multiple capacitive resistive sheets was presented which achieves a significant increase B/d in comparison to a traditional multilayer Jaumann absorber.

To investigate this effect, a Salisbury screen is modified to achieve similar performance from a thinner structure. In practice, this corresponds to constructing a thin sheet with a lattice of resistive patches, equivalent to a shunt resistance and capacitance in series as in Figure 4. The capacitance and conductance of this structure are given by

$$\alpha = \tan(k_0 d), \qquad C = \frac{1}{\eta\omega_0}\left(\alpha + \frac{1}{\alpha}\right), \qquad G = \frac{1}{\eta}\left(1 + \frac{1}{\alpha^2}\right) \qquad (5.1)$$

where ω_0 is the frequency of maximum absorption. The parameter α can be varied to control the response from the structure, as can be seen in Figure 11. As α decreases, the resonance of the absorber is shifted down in frequency, which corresponds to achieving similar performance as in the case of a regular Salisbury screen, but for a thinner absorber. As α decreases the bandwidth is slightly decreased. The curves in Figure 11 converge toward the planar case at approximately the same rate as the Salisbury screen in Figure 7, and there is no significant difference between the two normalizations. This indicates that both the original and the capacitively loaded Salisbury screen show a similar response with respect to curvature.

5.5   Circuit analog absorber

A simple case of a circuit analog absorber presented in [25] consists of a shunt series resistance, capacitance, and inductance, which could be realized as a periodic lattice of resistive patches. In this particular design, the circuit parameters are $R = 308\,\Omega$, $X = 30.8\,\text{fF}$, and $L = 3.16\,\text{nH}$, and the resistive sheet is placed a distance $\lambda_0/4$ from the ground plane, see [25] for further details on the specific absorber geometry and how to extract the circuit parameters from unit cell simulations. The results presented in Figure 12 indicate, compared to Figure 11, that the bandwidth is significantly improved by adding an inductive element L to the structure. However, this type of absorber might be quite difficult to manufacture in such a manner that the resistivity and reactance of the resistive sheet have the desired values.

5.6   Salisbury screen with a skin

In [6] it was shown that if a dielectric skin of a high dielectric constant is added outside of a Salisbury screen a double resonance occurs and the bandwidth of the absorber is improved. A planar absorber was designed in [6] according to the parameters in Figure 13, where a resistive sheet with $R = 225\,\Omega$ is placed a distance $d_1 = 6.8$ mm above a ground plane, and a dielectric skin of thickness 1 mm, and relative permittivity $\epsilon_\text{r} = 4$, is located a distance $d_2 = 2.3$ mm from the resistive
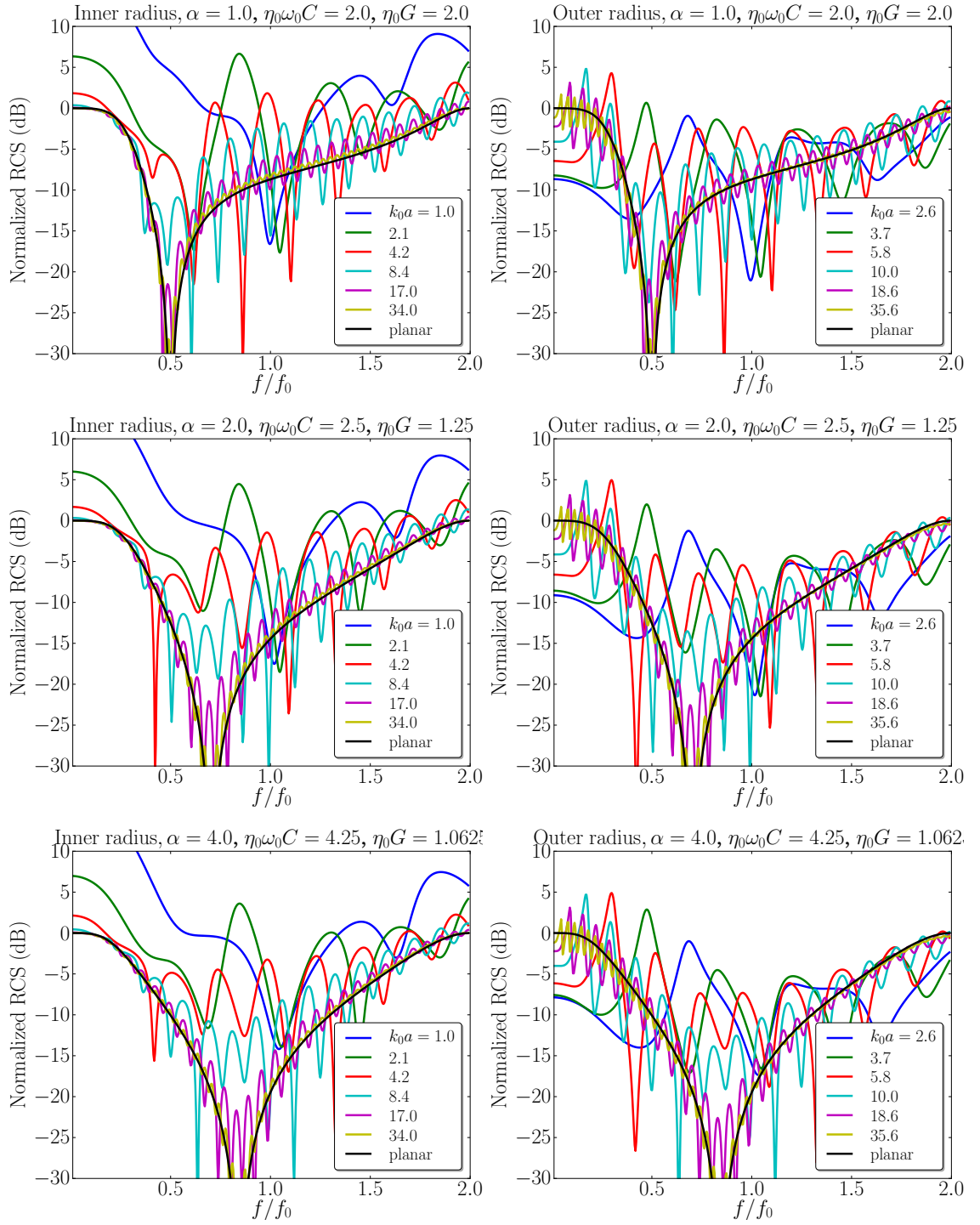
Figure 11: Monostatic RCS from a PEC sphere with a capacitive Salisbury screen, to the left normalized with the RCS of the inner PEC scatterer, and to the right normalized with the RCS of an enclosing PEC scatterer.

sheet. The total thickness of the absorber is 10.1 mm, which at the center frequency 7.42 GHz corresponds to approximately $\lambda_0/4$.
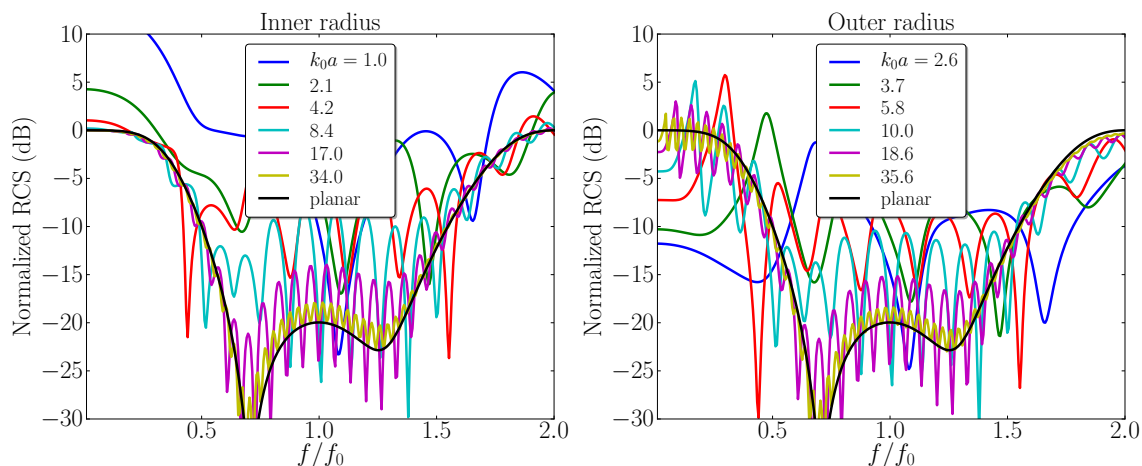
Figure 12: Monostatic RCS from a PEC sphere with a CAA screen from [25], to the left normalized with the RCS of the inner PEC scatterer, and to the right normalized with the RCS of an enclosing PEC scatterer.
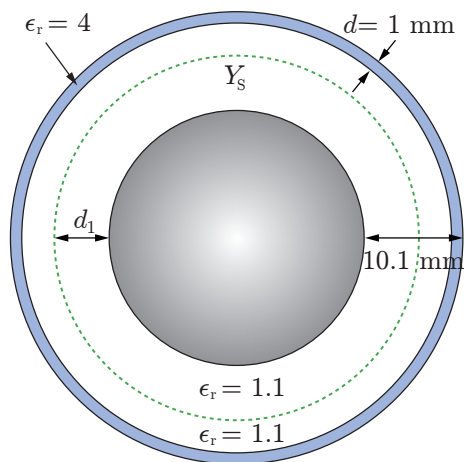

Figure 13: A PEC sphere coated by a resistive sheet and a dielectric skin commonly referred to as a Chambers-Tennant absorber.

This absorber design, henceforth referred to as a Chambers-Tennant absorber, was implemented as a coating for a spherical scatterer, and the results in Figure 14 indicate that, in conjecture to the previous absorber designs under study, the performance of the absorber does not converge towards that of the corresponding planar design for large scatterers. However, if losses are added to the spacer material the results in Figure 15 are achieved, where it can be seen that the results now converge better toward the planar curve. This is an indication of energy being stored in the spacer region as the structure acts as a spherical cavity, that resonates for the polarization component normal to the inner sphere surface.

5.7   Conductive volume absorber

In order to extent the study to absorbers based on bulk material losses, the resistive sheet and the spacer material inside the skin in Section 5.6 are replaced by a
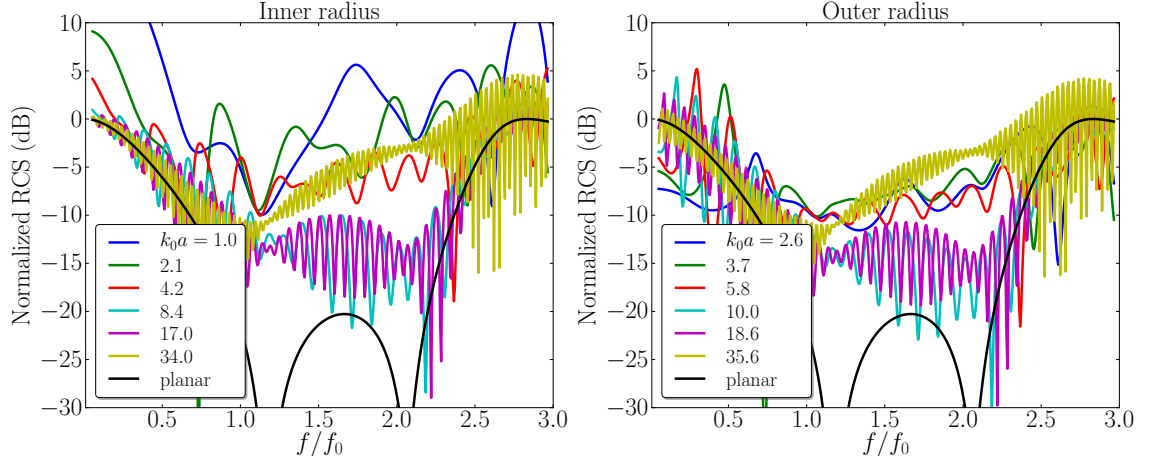
Figure 14: Monostatic RCS from a PEC sphere with a resistive sheet and a dielectric skin, to the left normalized with the RCS of the inner PEC scatterer, and to the right normalized with the RCS of an enclosing PEC scatterer.
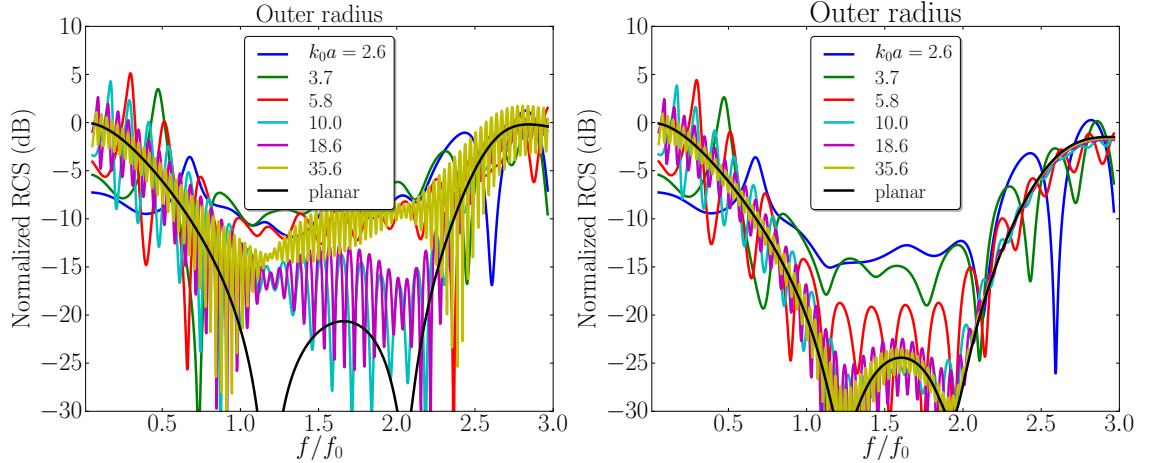

Figure 15: Monostatic RCS from a PEC sphere with a resistive sheet and a dielectric skin, where losses has been added to the spacer material, $\epsilon_{\rm r} = 1.1 - {\rm j}0.01$ (left) and $\epsilon_{\rm r} = 1.1 - {\rm j}0.1$ (right).

conducting bulk material with a relative permittivity on the form

$$\epsilon_{\rm r}(\omega) = \epsilon_{\rm r}' - {\rm j}\epsilon_{\rm r}''(\omega), \qquad \epsilon_{\rm r}' = A, \qquad \epsilon_{\rm r}''(\omega) = B\frac{\omega_0}{\omega}. \qquad (5.2)$$

The material parameters were chosen to be $A = 1.1$, $B = 2.39$ after a quick run in a simple optimization of the material parameters. The reflection coefficient was optimized of a planar absorber with respect to the threshold level -20 dB. This absorber was implemented in a spherical scenario as in see Figure 16 where the simulated geometry and the material parameters are presented. This type of volume (or bulk) absorber is seen in Figure 17 to perform very well when applied to a curved scatterer. This is an indication of the fact that the planar performance of

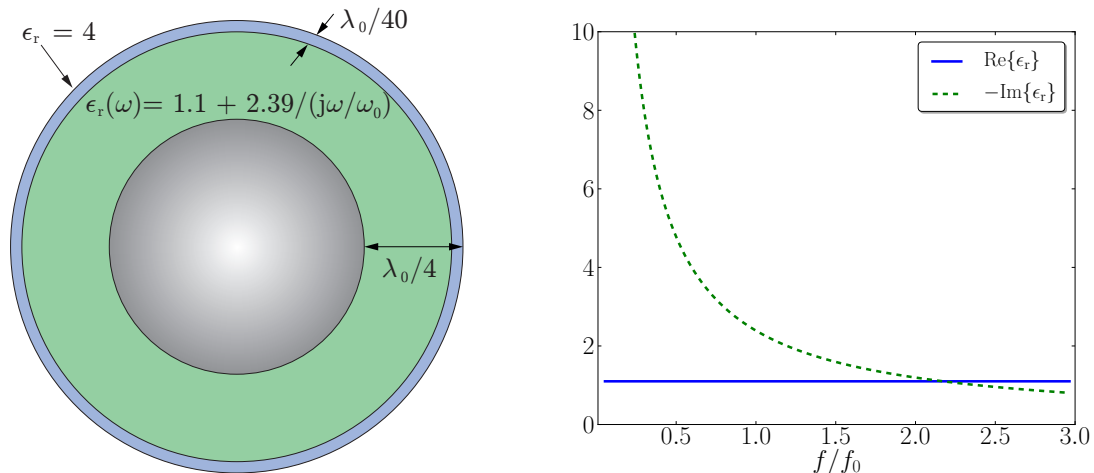this absorber can be used to anticipate the response from applying the absorber to a curved structure.

Figure 16: A PEC sphere coated by a volume absorber with a conducting bulk material and a skin (left) and the material parameters of the bulk material (right).
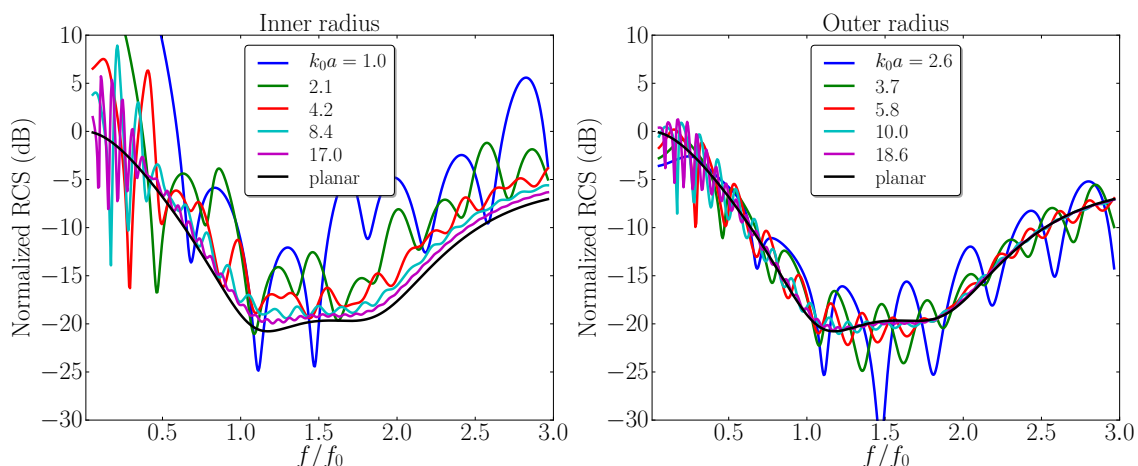

Figure 17: Monostatic RCS from a PEC sphere coated with a bulk absorber of a conducting material and a dielectric coating. To the left normalized with the RCS of the inner PEC scatterer, and to the right normalized with the RCS of an enclosing PEC scatterer.

5.8 Debye volume absorber

Now, we consider the geometry in Figure 18, which is the same setup as in the previous design, but with a Debye bulk material with a relative permittivity on the form

$$\epsilon_{\mathrm{r}}(\omega) = \epsilon_{\mathrm{r}}'(\omega) - \mathrm{j}\epsilon_{\mathrm{r}}''(\omega) = A + \frac{B}{\mathrm{j}\omega/\omega_0 + C} \tag{5.3}$$

where $A = 1$, $B = 2.39$, and $C = 0.13$ after performing the same type of optimization as in Section 5.7. The results in Figure 19 are very similar to those of the conductive bulk absorber in Figure 17, even though the material parameters in Figure 16 and Figure 18 can be seen to differ. The result curves in Figure 19 show a very good agreement to the planar design, even for relatively small spherical scatterers, where $k_0 a \approx 5$.
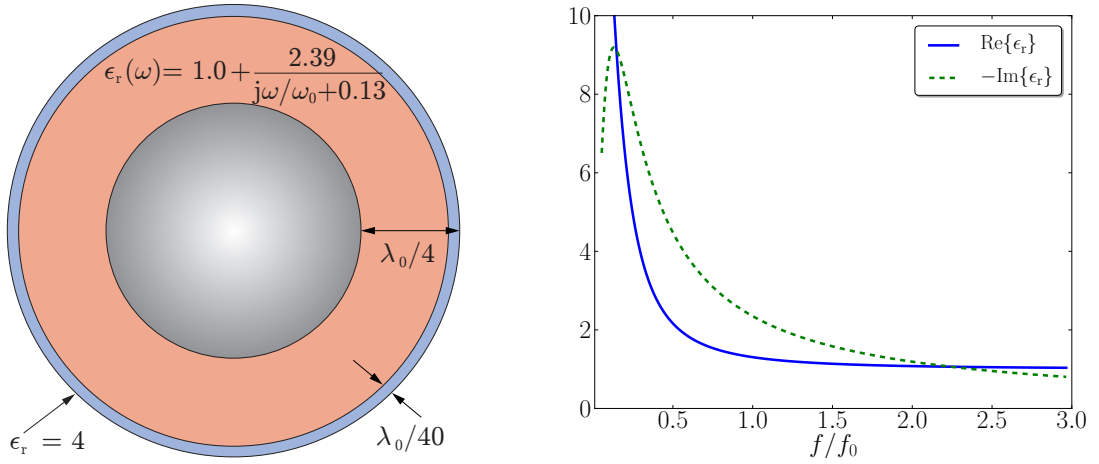

Figure 18: A PEC sphere coated by a volume absorber with a Debye bulk material and a skin (left) and the material parameters of the bulk material (right).
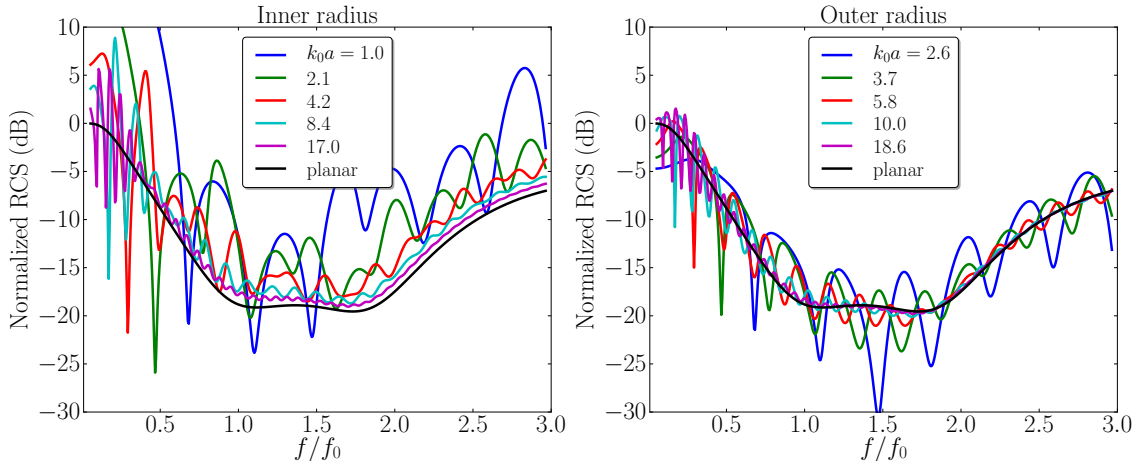

Figure 19: Monostatic RCS from a PEC sphere coated with a bulk absorber of a Debye material, and a dielectric coating. To the left normalized with the RCS of the inner PEC scatterer, and to the right normalized with the RCS of an enclosing PEC scatterer.

5.9   Thin magnetic sheet absorber

The final absorber under study is a thin magnetic sheet absorber, as in Figure 20. The absorber has a thickness of $d = \lambda_0/20$ and relative permittivity and relative permeability given by

$$\epsilon_\mathrm{r}(\omega) = \epsilon_\mathrm{r}'(\omega) - \mathrm{j}\epsilon_\mathrm{r}''(\omega) = 10 + \frac{0.05}{\mathrm{j}\omega/\omega_0 + 1.0}$$

$$\mu_\mathrm{r}(\omega) = \mu_\mathrm{r}'(\omega) - \mathrm{j}\mu_\mathrm{r}''(\omega) = 1.0 + \frac{1.1}{\mathrm{j}\omega/\omega_0 + 0.5},$$

after performing the same type of optimization as in Section 5.7. The results presented in Figure 21 indicate that this absorber is well suited for applications of cloaking curved surfaces, as the curves converge to the planar results for relatively small radii of curvature, $k_0 a \approx 5$. The resonance in Figure 21 can be seen to be shifted up in frequency compared to the Salisbury screen, although B/d quite large for this type of absorber in relation to the previous designs in this work.
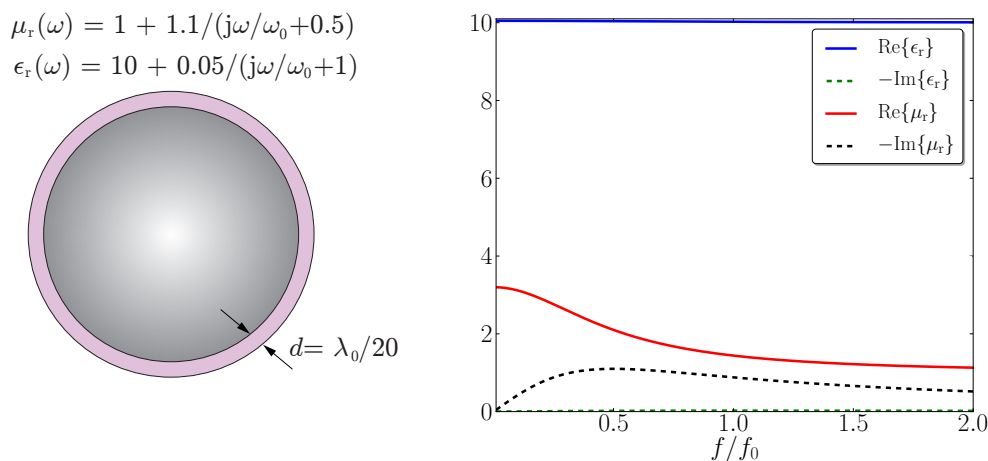

Figure 20: A PEC sphere coated by a thin magnetic absorber (left) and the material parameters of the absorber (right).
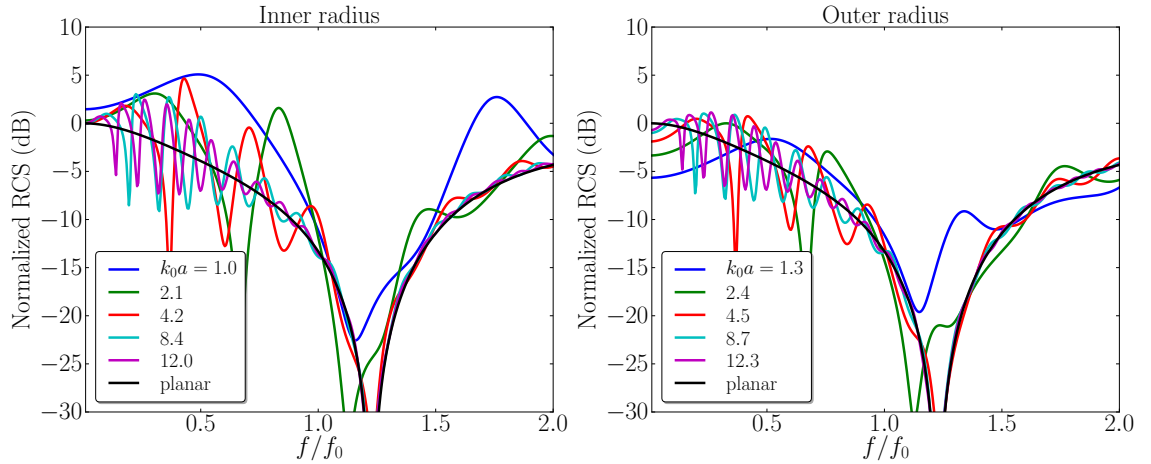
Figure 21: Monostatic RCS from a PEC sphere coated with thin magnetic material absorber. To the left normalized with the RCS of the inner PEC scatterer, and to the right normalized with the RCS of an enclosing PEC scatterer.

5.10   Evaluation of absorber performance

The results in Section 5 are summarized in Table 1, where the values of ka for the different types of absorbers correspond to a rough estimate of when the difference in absorber performance of the spherical and planar scenario is $< 3\,\mathrm{dB}$, in the case of normalization with enclosing PEC. A general observation of the results are that the normalized RCS of a PEC sphere coated with an absorber converges to the planar scattering parameter of the absorber backed by a ground plane, when the radius of the PEC sphere is increased to a few wavelengths in size. This is true for all absorbers in this study except for the Chambers-Tennant absorber in Section 5.6, where it was observed that the PEC sphere and absorber act as a spherical cavity which reduces the absorber performance. When comparing the results in

Absorber	Sphere size (ka)
Salisbury	17
Capacitive Salisbury	17
CAA	25
Jaumann	60
Chambers-Tennant	-
Conductive bulk	5
Debye bulk	5
Thin magnetic	6

Table 1: Summary of when the monostatic scattering of a sphere coated by an absorber has converged to the planar scattering parameter.

Table 1 to the similar analysis presented in [26] it is noted that the convergence of the absorber performance in a sphere scattering scenario is comparable to that

of the TM component of an absorber applied to a cylinder of infinite extent in the axial direction. At the same time, the TE component in the cylinder scattering scenario in [26] converges significantly faster when ka is increased. This conclusion implies that the performance of electromagnetic absorbers is relatively insensitive to curvature in the TE-direction of the incident signal, while curvature in the TM direction with respect to the incident signal has a more significant effect on the absorber performance.

When comparing the results in Section 5 using the "inner" or "outer" normalization scheme it can be seen that the outer normalization seems to overestimate the absorber performance, while the inner normalization underestimates the absorber performance. This effect is especially noticeable for the Jaumann absorber in Section 5.3. Which normalization technique that is preferable depends on the application where the absorber is used. For example, in some applications the outer dimensions of the object, with an absorber applied, are predetermined and in these cases the outer normalization is most relevant. On the other hand, if the inner dimensions of the scatterer are predefined the inner normalization gives a more realistic evaluation of the absorber performance in the current scenario.

6 Conclusions

A method for calculating the electromagnetic scattering from a multilayer spherical scatterer, possibly resistive sheets at the interfaces, has been presented. The solution to the specific scattering problem is a recursion relation of the transition matrix elements, on the form of a Möbius transform. From the transition matrix components the scattered fields can be calculated in any direction. A numerical implementation of the solution has been implemented, resulting in a code that can handle any number of layers, resistive sheets, lossy electric and magnetic materials, and dispersive materials and sheets.

A number of different electromagnetic absorbers have been applied to spherical scatterers of different size, and the effect of curvature on the absorber performance was evaluated. By normalizing the scattering from a coated scatterer with, either the scattering from the uncoated structure, or an enclosing PEC structure, a comparison can be made between the absorber performance of the curved application and a corresponding planar design. It is concluded that absorbers based on resistive sheets or circuit analog layers, are more sensitive to curvature than bulk absorbers, based on volume losses, such as thin magnetic absorbers or carbon doped dielectric absorbers.

It has also been observed that the convergence of the absorber performance in a sphere scattering scenario is comparable to that of the TM component of an absorber applied to a cylinder of infinite extent in the axial direction [26], while the TE component converges much faster when ka is increased. This implies that the performance of electromagnetic absorbers is relatively insensitive to curvature in the TE direction of the incident signal, while curvature in the TM direction with respect to the incident signal has a more significant effect on the absorber performance.

Appendix A Derivation of T-matrix components for plane wave illumination of a layered sphere

As was stated in Section 3.5, the total fields in each region of a layered sphere are given by (3.29) and the boundary conditions at each interfaces of the layered sphere are presented in (3.30). If the fields in (3.29) are inserted in (3.30), the first expression in (3.30) results in the relations

$$A_{1n}^{(i)}(j_l(k_i r_i) + t_{1l}^{(i-1)} h_l^{(2)}(k_i r_i)) = A_{1n}^{(i+1)}(j_l(k_{i+1} r_i) + t_{1l}^{(i)} h_l^{(2)}(k_{i+1} r_i)) \tag{6.1}$$

$$A_{2n}^{(i)} \left(\frac{(k_i r_i j_l(k_i r_i))'}{k_i r_i} + t_{2l}^{(i-1)} \frac{(k_i r_i h_l^{(2)}(k_i r_i))'}{k_i r_i} \right) =$$
$$A_{2n}^{(i+1)} \left(\frac{(k_{i+1} r_i j_l(k_{i+1} r_i))'}{k_{i+1} r_i} + t_{2l}^{(i)} \frac{(k_{i+1} r_i h_l^{(2)}(k_{i+1} r_i))'}{k_{i+1} r_i} \right), \tag{6.2}$$

and the second relation in (3.30) results in the expressions

$$A_{1n}^{(i)} \frac{1}{\eta_i} \left(\frac{(k_i r_i j_l(k_i r_i))'}{k_i r_i} + t_{2l}^{(i-1)} \frac{(k_i r_i h_l^{(2)}(k_i r_i))'}{k_i r_i} \right)$$
$$- A_{1n}^{(i+1)} \frac{1}{\eta_{i+1}} \left(\frac{(k_{i+1} r_i j_l(k_{i+1} r_i))'}{k_{i+1} r_i} + t_{2l}^{(i)} \frac{(k_{i+1} r_i h_l^{(2)}(k_{i+1} r_i))'}{k_{i+1} r_i} \right)$$
$$= -jY_S^{(i)} A_{1n}^{(i)}(j_l(k_i r_i) + t_{1l}^{(i)} h_l^{(2)}(k_i r_i)) \tag{6.3}$$

$$A_{2n}^{(i)} \frac{1}{\eta_i} \left(j_l(k_i r_i) + t_{2l}^{(i-1)} h_l^{(2)}(k_i r_i) \right) - A_{2n}^{(i+1)} \frac{1}{\eta_{i+1}} \left(j_l(k_{i+1} r_i) + t_{2l}^{(i)} h_l^{(2)}(k_{i+1} r_i) \right)$$
$$= jY_S^{(i)} A_{2n}^{(i)} \left(\frac{(k_i r_i j_l(k_i r_i))'}{k_i r_i} + t_{2l}^{(i-1)} \frac{(k_i r_i h_l^{(2)}(k_i r_i))'}{k_i r_i} \right), \tag{6.4}$$

where we have used the relations

$$\hat{r} \times \boldsymbol{A}_{3n}(\hat{r}) = \boldsymbol{0}, \quad \boldsymbol{A}_{2n}(\hat{r}) = \hat{r} \times \boldsymbol{A}_{1n}(\hat{r}), \quad \boldsymbol{A}_{1n}(\hat{r}) = \boldsymbol{A}_{2n}(\hat{r}) \times \hat{r}. \tag{6.5}$$

The goal from here is to eliminate all the the coefficients $A_{\tau n}$, and to find recursion expressions for the unknown T-matrix coefficients $t_{\tau l}^{(i)}$. To simplify the notation further, introduce the Riccati-Bessel functions and their derivatives [1, 19]

$$\begin{aligned} \psi_l(z) &= z j_l(z), & \xi_l(z) &= z h_l^{(2)}(z) \\ \psi_l'(z) &= j_l(z) + z j_l'(z), & \xi_l'(z) &= h_l^{(2)}(z) + z h_l'^{(2)}(z), \end{aligned} \tag{6.6}$$

and divide (6.4) by (6.2) to get the expression

$$\frac{\frac{1}{\eta_i}(\psi_l(k_ir_i) + t_{2l}^{(i-1)}\xi_l(k_ir_i)) - \mathrm{j}Y_{\mathrm{S}}^{(i)}(\psi_l'(k_ir_i) + t_{2l}^{(i-1)}\xi_l'(k_ir_i))}{\psi_l'(k_ir_i) + t_{2l}^{(i-1)}\xi_l'(k_ir_i)}$$

$$= \frac{1}{\eta_{i+1}}\left(\frac{\psi_l(k_{i+1}r_i) + t_{2l}^{(i)}\xi_l(k_{i+1}r_i)}{\psi_l'(k_{i+1}r_i) + t_{2l}^{(i)}\xi_l'(k_{i+1}r_i)}\right). \quad (6.7)$$

Now, divide (6.3) by (6.1), to get

$$\frac{\frac{1}{\eta_i}(\psi_l'(k_ir_i) + t_{1l}^{(i-1)}\xi_l'(k_ir_i)) + \mathrm{j}\eta_i Y_{\mathrm{S}}^{(i)}(\psi_l(k_ir_i) + t_{1l}^{(i-1)}\xi_l(k_ir_i))}{\psi_l(k_ir_i) + t_{1l}^{(i-1)}\xi_l(k_ir_i)}$$

$$= \frac{1}{\eta_{i+1}}\left(\frac{\psi_l'(k_{i+1}r_i) + t_{1l}^{(i)}\xi_l'(k_{i+1}r_i)}{\psi_l(k_{i+1}r_i) + t_{1l}^{(i)}\xi_l(k_{i+1}r_i)}\right), \quad (6.8)$$

where it can be seen that (6.7) only contain the T-matrix components $t_{1l}^{(i-1)}$, $t_{1l}^{(i)}$, and (6.8) only contain the T-matrix component $t_{2l}^{(i-1)}$, $t_{2l}^{(i)}$. Furthermore, the expressions (6.7)-(6.8) describe recursion relations where the unknown T-matrix components are updated for each layer through linear mappings $A(\cdot)$, $B(\cdot)$

$$\begin{cases} t_{1l}^{(i)} = A(t_{1l}^{(i-1)}) \\ t_{2l}^{(i)} = B(t_{2l}^{(i-1)}) \end{cases} \qquad i = 1, 2, ..., n+1. \quad (6.9)$$

These mappings can be seen to have the general structure

$$\frac{a' + b'x_1}{c' + d'x_1} = \frac{e' + f'x_2}{g' + h'x_2} \quad (6.10)$$

where $a', b', c', d', e', f', g'$ and h' are known coefficients, and x_1 is a known parameter and x_2 is unknown. A rearrangement of (6.10) results in the familiar Möbius transform

$$x_2 = \frac{(e'd' - b'g')x_1 + e'c' - a'g'}{(b'h' - f'd')x_1 + a'h' - f'c'} = -\frac{ax_1 + b}{cx_1 + d}, \quad (6.11)$$

where,

$$\begin{aligned} a &= b'g' - e'd' & b &= a'g' - e'c' \\ c &= b'h' - f'd' & d &= a'h' - f'c'. \end{aligned} \quad (6.12)$$

This implies that by identifying the exact expressions of $a', b', c', d', e', f', g'$ and h' for our two expressions (6.7)-(6.8), we have a final expression for the solution to the problem. In (6.7) the mapping coefficients are

$$\begin{aligned} a' &= \frac{\eta_{i+1}}{\eta_i}\psi_l(k_ir_i) - \mathrm{j}Y_{\mathrm{S}}^{(i)}\psi_l'(k_ir_i)\eta_{i+1} & b' &= \frac{\eta_{i+1}}{\eta_i}\xi_l(k_ir_i) - \mathrm{j}Y_{\mathrm{S}}^{(i)}\xi_l'(k_ir_i)\eta_{i+1} \\ c' &= \psi_l'(k_ir_i) & d' &= \xi_l'(k_ir_i) \\ e' &= \psi_l(k_{i+1}r_i) & f' &= \xi_l(k_{i+1}r_i) \\ g' &= \psi_l'(k_{i+1}r_i) & h' &= \xi_l'(k_{i+1}r_i), \end{aligned} \quad (6.13)$$

and in (6.8) the mapping coefficients are

$$
\begin{aligned}
a' &= \frac{\eta_{i+1}}{\eta_i}\psi_l'(k_ir_i) - \mathrm{j}Y_{\mathrm{S}}^{(i)}\psi_l(k_ir_i)\eta_{i+1} & b' &= \frac{\eta_{i+1}}{\eta_i}\xi_l'(k_ir_i) - \mathrm{j}Y_{\mathrm{S}}^{(i)}\xi_l(k_ir_i)\eta_{i+1} \\
c' &= \psi_l(k_ir_i) & d' &= \xi_l(k_ir_i) \\
e' &= \psi_l'(k_{i+1}r_i) & f' &= \xi_l'(k_{i+1}r_i) \\
g' &= \psi_l(k_{i+1}r_i) & h' &= \xi_l(k_{i+1}r_i).
\end{aligned}
\tag{6.14}
$$

Finally, the recursive expression for the T-matrix coefficients can be formulated as

$$
t_{\tau l}^{(i)} = -\frac{a_\tau^{(i)}t_{\tau l}^{(i-1)} + b_\tau^{(i)}}{c_\tau^{(i)}t_{\tau l}^{(i-1)} + d_\tau^{(i)}},
\tag{6.15}
$$

where for $\tau = 1$ the coefficients are

$$
\begin{cases}
a_1^{(i)} = \dfrac{\eta_i}{\eta_{i+1}}\xi_l(k_ir_i)\psi_l'(k_{i+1}r_i) - \xi_l'(k_ir_i)\psi_l(k_{i+1}r_i) - \mathrm{j}\eta_iY_{\mathrm{S}}^{(i)}\xi_l(k_ir_i)\psi_l(k_{i+1}r_i) \\[2mm]
b_1^{(i)} = \dfrac{\eta_i}{\eta_{i+1}}\psi_l(k_ir_i)\psi_l'(k_{i+1}r_i) - \psi_l'(k_ir_i)\psi_l(k_{i+1}r_i) - \mathrm{j}\eta_iY_{\mathrm{S}}^{(i)}\psi_l(k_ir_i)\psi_l(k_{i+1}r_i) \\[2mm]
c_1^{(i)} = \dfrac{\eta_i}{\eta_{i+1}}\xi_l(k_ir_i)\xi_l'(k_{i+1}r_i) - \xi_l'(k_ir_i)\xi_l(k_{i+1}r_i) - \mathrm{j}\eta_iY_{\mathrm{S}}^{(i)}\xi_l(k_ir_i)\xi_l(k_{i+1}r_i) \\[2mm]
d_1^{(i)} = \dfrac{\eta_i}{\eta_{i+1}}\psi_l(k_ir_i)\xi_l'(k_{i+1}r_i) - \psi_l'(k_ir_i)\xi_l(k_{i+1}r_i) - \mathrm{j}\eta_iY_{\mathrm{S}}^{(i)}\psi_l(k_ir_i)\xi_l(k_{i+1}r_i),
\end{cases}
\tag{6.16}
$$

and for $\tau = 2$ the coefficients are

$$
\begin{cases}
a_2^{(i)} = \dfrac{\eta_{i+1}}{\eta_i}\xi_l(k_ir_i)\psi_l'(k_{i+1}r_i) - \xi_l'(k_ir_i)\psi_l(k_{i+1}r_i) - \mathrm{j}\eta_{i+1}Y_{\mathrm{S}}^{(i)}\xi_l'(k_ir_i)\psi_l'(k_{i+1}r_i) \\[2mm]
b_2^{(i)} = \dfrac{\eta_{i+1}}{\eta_i}\psi_l(k_ir_i)\psi_l'(k_{i+1}r_i) - \psi_l'(k_ir_i)\psi_l(k_{i+1}r_i) - \mathrm{j}\eta_{i+1}Y_{\mathrm{S}}^{(i)}\psi_l'(k_ir_i)\psi_l'(k_{i+1}r_i) \\[2mm]
c_2^{(i)} = \dfrac{\eta_{i+1}}{\eta_i}\xi_l(k_ir_i)\xi_l'(k_{i+1}r_i) - \xi_l'(k_ir_i)\xi_l(k_{i+1}r_i) - \mathrm{j}\eta_{i+1}Y_{\mathrm{S}}^{(i)}\xi_l'(k_ir_i)\xi_l'(k_{i+1}r_i) \\[2mm]
d_2^{(i)} = \dfrac{\eta_{i+1}}{\eta_i}\psi_l(k_ir_i)\xi_l'(k_{i+1}r_i) - \psi_l'(k_ir_i)\xi_l(k_{i+1}r_i) - \mathrm{j}\eta_{i+1}Y_{\mathrm{S}}^{(i)}\psi_l'(k_ir_i)\xi_l'(k_{i+1}r_i).
\end{cases}
\tag{6.17}
$$

For the case of a general material at the center of the scatterer, the iteration starts by $i = 1$. However, If the innermost layer is a PEC then the iteration starts at $i = 2$, and it is initialized by

$$
t_{1l}^{(i)} = \frac{\psi_l(k_2r_1)}{\xi_l(k_2r_1)}, \qquad t_{2l}^{(i)} = \frac{\psi_l'(k_2r_1)}{\xi_l'(k_2r_1)}.
\tag{6.18}
$$

Appendix B Verification of numerical implementation

In this section the monostatic RCS of differerent scatterers is calculated using the implemented code and a number of commercial software.
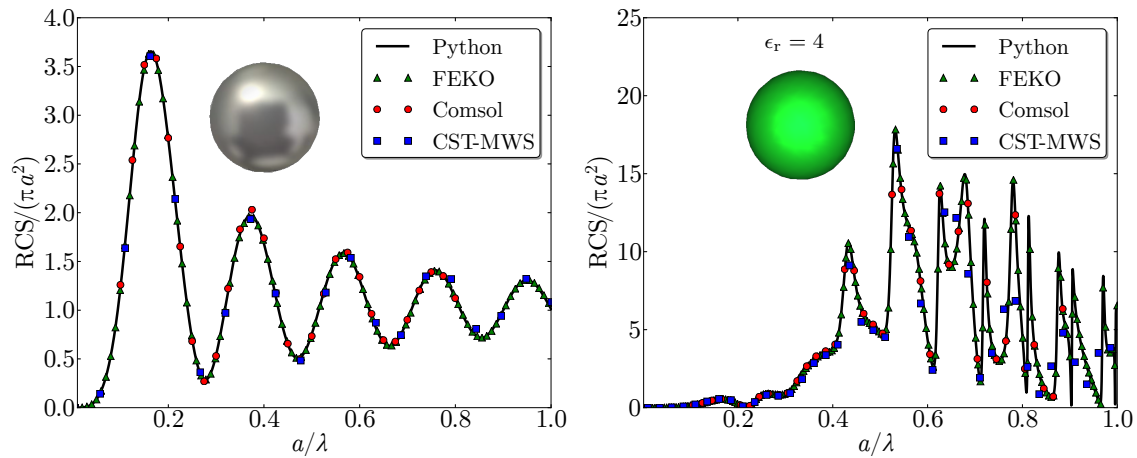
Figure 22: Verification simulations of the monostatic RCS of a PEC sphere (left) and a dielectric sphere of relative permittivity $\epsilon_r = 4$ (right), calculated using the numerical code implemented in Python in this work, the MoM solver in FEKO, and the FEM solver in CST-MWS and Comsol Multiphysics.
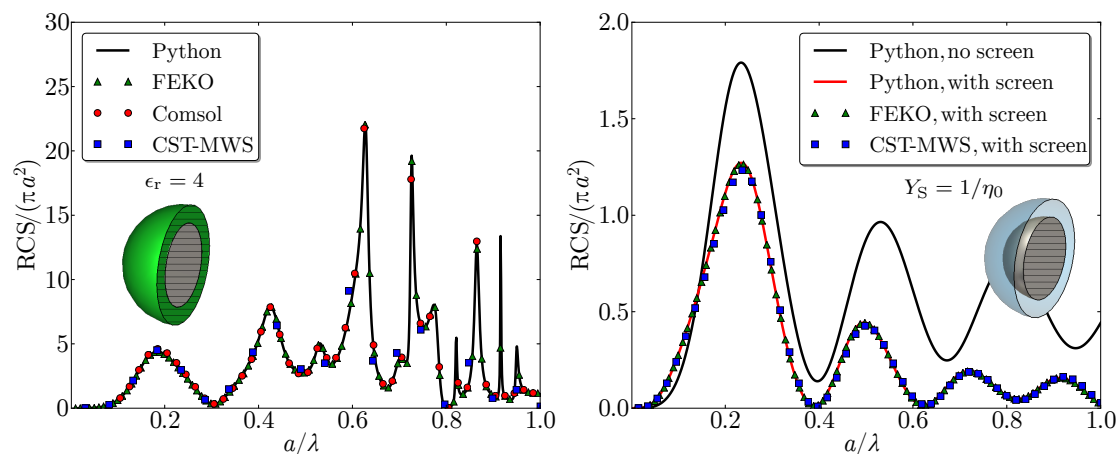

Figure 23: Verification simulations of the monostatic RCS of a PEC sphere coated with a dielectric shell (left) and a PEC sphere with a resistive sheet (right), calculated using the numerical code implemented in Python in this work, the MoM solver in FEKO, and the FEM solver in CST-MWS and Comsol Multiphysics. The outer radius of the spheres is a. In the left scenario the PEC sphere radius is $0.7a$, the dielectric shell has a relative permittivity $\epsilon_r = 4$ and thickness $d = 0.3a$. In the right scenario the PEC sphere has the radius $0.7a$ and the resistive coating is located a distance $d = 0.3a$ from the sphere.
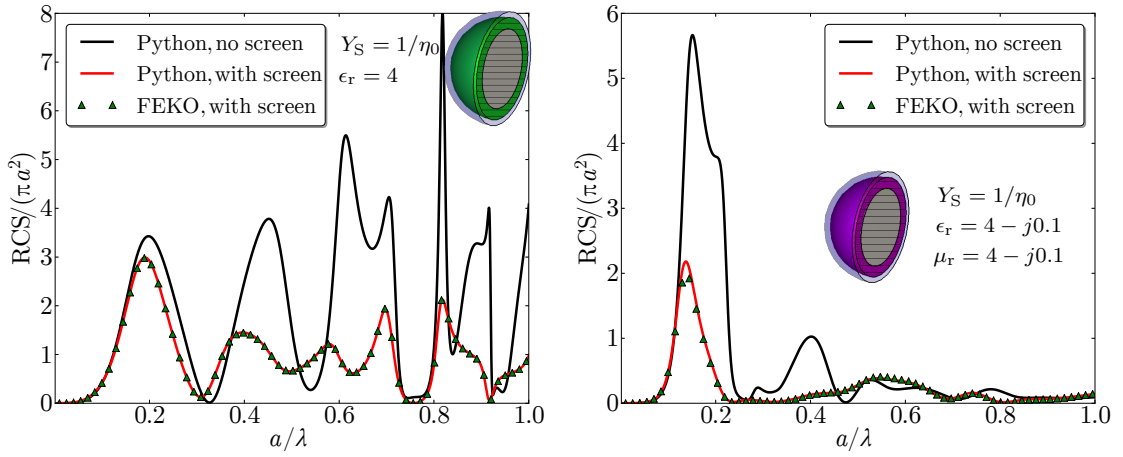
Figure 24: Verification simulations of the monostatic RCS for a PEC sphere with a dielectric coating and a resistive sheet (left), and a PEC sphere with a magnetic lossy coating and a resistive sheet (right), calculated using the numerical code implemented in Python in this work and the MoM solver in FEKO. The outer radius of the spheres is a. In the left scenario the PEC sphere has radius $0.7a$, the dielectric shell has a relative permittivity $\epsilon_{\mathrm{r}} = 4$ and thickness $d = 0.2a$ and the resistive coating is located a distance $d = 0.1a$ from the dielectric layer. In the right scenario the PEC sphere has radius $0.7a$, the magnetic shell has the relative permeability $\mu_{\mathrm{r}} = 4 - 0.1\mathrm{j}$, relative permittivity $\epsilon_{\mathrm{r}} = 4 - 0.1\mathrm{j}$ and thickness $d = 0.2a$ and the resistive coating is located a distance $d = 0.1a$ from the magnetic layer.

References

[1] M. Abramowitz and I. A. Stegun, eds. "Handbook of Mathematical Functions". Applied Mathematics Series No. 55. National Bureau of Standards, 1970.

[2] C. F. Bohren and D. R. Huffman. "Absorption and Scattering of Light by Small Particles". John Wiley & Sons, 1983.

[3] J. J. Bowman, T. B. A. Senior, and P. L. E. Uslenghi. "Electromagnetic and Acoustic Scattering by Simple Shapes". North-Holland, 1969.

[4] J. J. Bowman and V. H. Weston. "The effect of curvature on the reflection coefficient of layered absorbers". *IEEE Trans. Antennas Propag.* 14 (6) (1966): pp. 760–767.

[5] C. Cantrell. *Numerical methods for the accurate calculation of spherical Bessel functions and the location of Mie resonances*. 2013, Accessed: 2017-02-18.

[6] B. Chambers and A. Tennant. "Design of wideband Jaumann radar absorbers with optimum oblique incidence performance". *Electronics Letters* 30 (18) (1994): pp. 1530–1532.

[7] J. Dave. *Subroutines for computing the parameters of the electromagnetic radiation scattered by a sphere*. Tech. rep. No. 320-3237. IBM Palo Alto Scientific Center, Calif., 1968.

[8] A. Ericsson, D. Sjöberg, C. Larsson, and T. Martin. "Scattering for doubly curved functional surfaces and corresponding planar designs". In: *Antennas and Propagation (EuCAP), 2016 10th European Conference on*. IEEE. 2016, pp. 1–2.

[9] A. Gogoi, A. Choudhury, and G. A. Ahmed. "Mie scattering computation of spherical particles with very large size parameters using an improved program with variable speed and accuracy". *Journal of Modern Optics* 57 (21) (2010): pp. 2192–2202.

[10] W. Hergert and T. Wriedt. "The Mie Theory: Basics and Applications". Vol. 169. Springer, 2012.

[11] A. Kazemzadeh and A. Karlsson. "Multilayered wideband absorbers for oblique angle of incidence". *IEEE Trans. Antennas Propag.* 58 (11) (2010): pp. 3637–3646.

[12] E. F. Knott and K.Langseth. "Performance degardation of Jaumann absorbers due to curvature". *IEEE Trans. Antennas Propag.* 28 (1) (1980): pp. 137–139.

[13] E. F. Knott, J. F. Shaeffer, and M. T. Tuley. "Radar Cross Section". SciTech Publishing Inc., 2004.

[14] G. Kristensson. "Scattering of Electromagnetic Waves by Obstacles". SciTech Publishing, an imprint of the IET, 2016.

[15] W. J. Lentz. "Generating Bessel functions in Mie scattering calculations using continued fractions". *Applied Optics* 15 (3) (1976): pp. 668–671.

[16] G. Mie. "Beiträge zur Optik trüber Medien, speziell kolloidaler Metallösungen". *Ann. Phys. Leipzig* 25 (1908): pp. 377–445.

[17] M. I. Mishchenko and L. D. Travis. "Gustav mie and the evolving discipline of electromagnetic scattering by particles". *Bulletin of the American Meteorological Society* 89 (12) (2008): pp. 1853–1861.

[18] B. Munk. "Frequency Selective Surfaces: Theory and Design". John Wiley & Sons, 2000.

[19] F. W. J. Olver, D. W. Lozier, R. F. Boisvert, and C. W. Clark. "NIST Handbook of mathematical functions". Cambridge University Press, 2010.

[20] K. N. Rozanov. "Ultimate thickness to bandwidth ratio of radar absorbers". *IEEE Trans. Antennas Propag.* 48 (8) (2000): pp. 1230–1234.

[21] G. T. Ruck, D. E. Barrick, W. D. Stuart, and C. K. Krichbaum. "Radar Cross-Section Handbook". Vol. 1 and 2. Plenum Press, 1970.

[22] W. Salisbury. *Absorbent body for electromagnetic waves.* 1952.

[23] J. Shen and X. Cai. "Algorithm of numerical calculation on Lorentz Mie theory". *PIERS Online* 1 (6) (2005): pp. 691–694.

[24] R. A. Shore. "Scattering of an electromagnetic linearly polarized plane wave by a multilayered sphere: obtaining a computational form of mie coefficients for the scattered field." *Antennas and Propagation Magazine, IEEE* 57 (6) (2015): pp. 69–116.

[25] D. Sjöberg. "Circuit analogs for wave propagation in stratified structures". In: *Wave Propagation in Materials for Modern Applications.* Ed. by A. Petrin. InTech, 2010, pp. 489–508.

[26] D. Sjöberg. "Scattering for singly curved functional surfaces and corresponding planar designs". In: *Antennas and Propagation (EuCAP), 2013 7th European Conference on.* IEEE. 2013, pp. 3339–3342.

[27] J. A. Stratton. "Electromagnetic Theory". McGraw-Hill, 1941.

[28] J. W. Strutt. "Lviii. on the scattering of light by small particles". *The London, Edinburgh, and Dublin Philosophical Magazine and Journal of Science* 41 (275) (1871): pp. 447–454.

[29] H. E. William. "Electromagnetic wave absorbers and anechoic chambers through the years". *IEEE Trans. Antennas Propag.* 21 (4) (1973).

[30] W. J. Wiscombe. "Improved Mie scattering algorithms". *Applied optics* 19 (9) (1980): pp. 1505–1509.